Graduate School ETD Form 9
(Revised 12/07)

PURDUE UNIVERSITY
GRADUATE SCHOOL
Thesis/Dissertation Acceptance

This is to certify that the thesis/dissertation prepared

By Azadeh Hemati

Entitled
LAYER BY LAYER NANOASSEMBLY OF COPPER INDIUM GALLIUM SELENIUM (CIGS) NANOPARTICLES FOR SOLAR CELL APPLICATION

For the degree of Master of Science in Mechanical Engineering

Is approved by the final examining committee:

Hazim El-Mounayri
Chair

Mangilal Agarwal

Kody Varahramyan

To the best of my knowledge and as understood by the student in the *Research Integrity and Copyright Disclaimer (Graduate School Form 20)*, this thesis/dissertation adheres to the provisions of Purdue University's "Policy on Integrity in Research" and the use of copyrighted material.

Approved by Major Professor(s): Hazim El-Mounayri

Approved by: Sohel Anwar 12/05/2011
Head of the Graduate Program Date

Graduate School Form 20
(Revised 9/10)

PURDUE UNIVERSITY
GRADUATE SCHOOL

Research Integrity and Copyright Disclaimer

Title of Thesis/Dissertation:

LAYER BY LAYER NANOASSEMBLY OF COPPER INDIUM GALLIUM SELENIUM (CIGS) NANOPARTICLES FOR SOLAR CELL APPLICATION

For the degree of Master of Science in Mechanical Engineering

I certify that in the preparation of this thesis, I have observed the provisions of *Purdue University Executive Memorandum No. C-22,* September 6, 1991, *Policy on Integrity in Research.**

Further, I certify that this work is free of plagiarism and all materials appearing in this thesis/dissertation have been properly quoted and attributed.

I certify that all copyrighted material incorporated into this thesis/dissertation is in compliance with the United States' copyright law and that I have received written permission from the copyright owners for my use of their work, which is beyond the scope of the law. I agree to indemnify and save harmless Purdue University from any and all claims that may be asserted or that may arise from any copyright violation.

Azadeh Hemati

Printed Name and Signature of Candidate

12/06/2011

Date (month/day/year)

*Located at http://www.purdue.edu/policies/pages/teach_res_outreach/c_22.html

LAYER BY LAYER NANOASSEMBLY OF COPPER INDIUM GALLIUM SELENIUM (CIGS) NANOPARTICLES FOR SOLAR CELL APPLICATION

A Thesis
Submitted to the Faculty
of
Purdue University
by
Azadeh Hemati

In Partial Fulfillment of the
Requirements for the Degree
of
Master of Science in Mechanical Engineering

December 2011
Purdue University
Indianapolis, Indiana

To
my parents,
who made all of this possible,
for their endless encouragement and patience

ACKNOWLEDGEMENTS

I would like to gratefully thank Dr. Kody Varahramyan and Dr. Mangilal Agarwal, for providing me the opportunity to be a part of this research, sharing their valuable knowledge and experiences with me, and advising me throughout this thesis work. And also Dr. Sudhir Shrestha, who taught me the research in a professional manner and showed me his pursuit of perfection in every single detail, for which I will always be thankful. I would like to thank Dr. Hazim El-Mounayri for chairing my advisory committee and helping me in many aspects of my academic success throughout these two years.

I am grateful to the Integrated Nanosystems Development Institute (INDI) at Indiana University Purdue University Indianapolis (IUPUI) for providing support and facilities for this research. I also thank Jason Cambridge for his contribution towards the synthesis and preparation of the nanoparticles for my research purpose, and appreciate my research group members, Parvin Ghane and Nojan Aliahmad for their helps, supports, and valuable contribution and discussions that led to successful completion of this thesis. I would also like to thank Mr. Rudy Earlson, Mr. Jeff Sears, and Mr. Cary Pritchard, for their technical support in the lab and Dr. Ricardo Decca for providing AFM, and Mr. Clif Duhn for running the SEM and EDS. I would also like to thank Ms. Valerie Lim Diemer and Ms. Ginger Jessop Lauderback for assisting me in formatting this thesis.

TABLE OF CONTENTS

Page

Page

LIST OF TABLES

LIST OF FIGURES

ABSTRACT

Hemati, Azadeh. M.S.M.E., Purdue University, December 2011. Layer by Layer Nanoassembly of Copper Indium Gallium Selenium (CIGS) Nanoparticles for Solar Cell Application. Major Professor: Hazim El-Mounayri.

In this research thesis, copper indium gallium selenium (CIGS) nanoparticles were synthesized from metal chlorides, functionalized to disperse in water, and further used in layer by layer (LbL) nanoassembly of CIGS films. CIGS nanoparticles were synthesized through the colloidal precipitation in an organic solvent. The peak and average sizes of the synthesized particles were measured to be 68 nm and 75 nm in chloroform, and 30 nm and 115 nm in water, respectively. Two methods were used to disperse the particle in water. In the first method the stabilizing agent oleylamine (OLA) was removed through multiple cleaning processes, and in the second method ligand exchange was performed with polystyrene sulfonate (PSS). Zeta potential of CIGS nanoparticles dispersed in water was measured to be +61 mV. The surface charge of the nanoparticles was reversed by raising the pH of the solution, which was measured to be −43.3 mV at 10.5 pH. In a separate process, the CIGS nanoparticles dispersed in water were coated with PSS. The resulting dispersion was observed to be stable and the surface charge was measured to be −56.9 mV.

The LbL deposition process of CIGS nanoparticles was characterized by depositing thin films on quartz crystal microbalance (QCM). LbL depositions was conducted using (i) oppositely charged CIGS nanoparticles, (ii) positively charged CIGS nanoparticles and PSS, and (iii) PSS-coated CIGS (CIGS-PSS) and polyethyleneimine

(PEI). The average thickness of each bi-layer of the above mentioned depositions were measured to be 2.2 nm, 1.37 nm, and 10.12 nm, respectively.

The results from the QCM have been observed to be consistent with the film thickness results obtained from atomic force microscopy (AFM). Various immersion times versus thickness of the film were also studied. For electrical characterization, the CIGS films were deposited on indium tindioxide (ITO)-coated glass substrates. Current versus voltage (I/V) measurements were carried out for each of the films using the Keithley semiconductor characterization instruments and micromanipulator probing station. It was observed that the conductivity of the films was increased with the deposition of each additional layer. The I/V characteristics were also measured under the light illumination and after annealing to study the photovoltaic and annealing effects. It was observed that under light illumination, the resistivity of a 12-layer CIGS film decreased by 93% to 0.54 MΩ.m, and that of the same number of layers of PSS-coated CIGS and PEI film decreased by 60% to 0.97 MΩ.m under illumination. The resistivity of an 8-layer CIGS and PSS film decreased by 76.4% to 0.1 MΩ.m, and that of the same layers of PSS-coated CIGS and PEI decreased by 87% to 0.07 MΩ.m after annealing.

The functionalized nanoparticles and the LbL CIGS films were implemented in the solar cell devices. Several configurations of CIGS films (p-type), and ZnO and CdS films (n-type) were considered. Poly(3,4-ethylenedioxythiophene) (PEDOT), molybdenum (Mo), and ITO were used as back contacts and ITO was used as front contact for all the devices. The devices were characterized the Keithley semiconductor characterization instruments and micromanipulator probing station. For a CIGS and n-ZnO films device with PEDOT as back contact and ITO as front contact, the current density at 0 V and under light illumination was measured to be 60 nA/cm^2 and the power density was measured to be 0.018 nW/cm^2. For a CIGS and CdS films device with ITO as both back and front contact, the current density at 0 V and under light illumination was measured to be 50 nA/cm^2 and the power density was measured to be 0.01 nW/cm^2. For a drop-casted CIGS and CdS films device with Mo as back contact and ITO as front

contact, the current density of 50 nA/cm^2 at 0 V and power density of 0.5 nW/cm^2 under light illumination was measured. For the LbL CIGS and chemical bath deposited CdS films device with ITO as both back and front contact, the current density of 0.04 mA/cm^2 at 0 V and power density of 1.6 μW/cm^2 under light illumination was measured. Comparing to Device-III, an increase by 99% in the power density was observed by using the CIGS LbL film in the device structure.

The novel aspects of this research include, (i) functionalization of the CIGS nanoparticles to disperse in water including coating with PSS, (ii) electrostatic LbL deposition of CIGS films using oppositely charged nanoparticles and polymers, and (iii) the utilization of the fabricated LbL CIGS films to develop solar cells. In addition, the n-type cadmium sulfide film (CdS) and zinc oxide (ZnO) buffer layer were also deposited through LbL process after the respective particles were functionalized with PSS coating in separate experiments.

1 INTRODUCTION

1.1 Background and Overview

The energy need of the United States and the world is growing every year. The current worldwide energy demand exceeds 13 TW and the world will need 30 TW power by 2050 [1]. To meet this growing of energy need, dependency on fossil fuel alone could not be sustainable both economically and environmentally. Thus, renewable and clean sources of energy, such as solar, wind, and geothermal have been pursued for a relatively long time. The prices of the renewable energy sources have been declining over the years, however, to become commercially competent with fossil fuels, the prices of the renewable energy have to be reduced further and the efficiencies have to be improved significantly. The growing demand of world energy and the diminishing fossil fuel reserves are helping drive the cost of energy higher every year. This along with the improved renewable energy sources will ultimately lead to a viable sustainable renewable energy generation. In addition, the effects of the emissions have been shown to be devastating to our environment. Therefore, energy security and global climate change will be the main agenda in the coming decades.

Among the above mentioned clean sources of energy, the sun has the ability to produce roughly 120,000 TW of solar energy every day. Moreover, solar cells are safe and have much less hazardous effects to the environment while reducing the carbon emissions. Due to the above explanations solar has been the fastest growing industry in the past decade. The solar cells and photovoltaic (PV) systems production has been doubled every two years since 2002. Japan, Europe, and the USA are the three foremost countries providing about 89% of the worldwide PV capacity [2]. In Figure 1.1.1, the yearly growth of solar energy usage is shown.

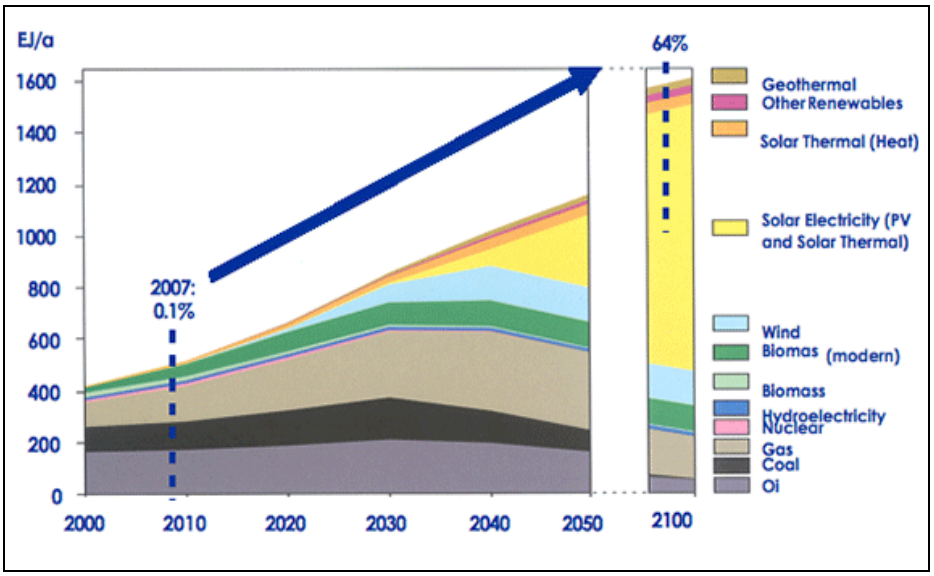

Figure 1.1.1 Yearly consumption of energy by source [3]

A solar cell is a solid state electrical device in which solar energy is converted into electrical energy via the photovoltaic effect. The photovoltaic term comes from two words, “Photo” means “light”, and “voltaic” comes from the name of an Italian physicist Volta. The photo-voltaic effect was first found by a French physicist, A. E. Becquerel, in 1839 [4] but the first photovoltaic cell was built in 1883 by Charles Fritts [5], who built the first photovoltaic cell, made junctions by coating a very thin thin layer of gold on top of the selenium semiconductor. The efficiency outcome of this cell was about 1%. In 1888, the first photoelectric cell was built by Aleksandr Stoletov based on the outer photoelectric effect discovered by Henrich Hertz.

In 1905, the photoelectric effect was described by Albert Einstein which led to the Nobel Prize in physics for him in 1921. Solar cell was patented in 1946 by Russell Ohl, while working on a series of experiments on transistors. In 1954, the modern photovoltaic cell was developed at Bell laboratories and then Daryl Chapin, Calvin Souther Fuller and Gerald Pearson developed a highly efficient solar cell for the first time using diffused silicon p-n junction [6].

Currently, different types of solar cells are available in various categories. Solar cells categorized by their base components. They can be based on silicon, chemical compound or new materials. Each of these categories also includes some subdivisions. Figure 1.1.2 shows types of solar cells and also provides the market shares of each of them in year 2010.

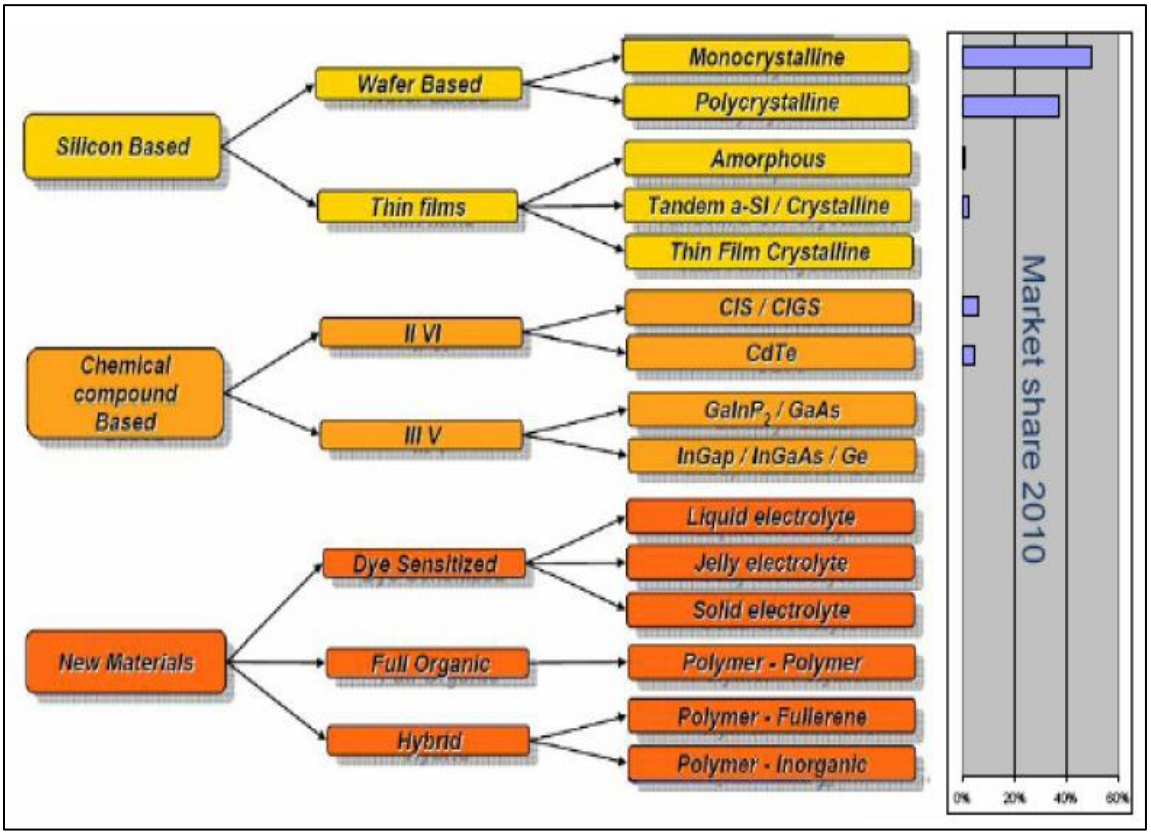

Figure 1.1.2 Market shares of various solar cells in 2010 [7]

Each type of the mentioned solar cells has different efficiencies and their efficiency has been improved during the time from primary solar cells in 1975 until now. The efficiency in solar cells is categorized in four different types named as thermodynamic, charge carrier separation, reflectance, and conductive efficiency. The overall efficiency is the combination of these individual efficiencies.

Figure 1.1.3 presents a comparison of laboratory efficiencies obtained for various materials in different types of solar cells from 1975 until 2010. Commercial efficiencies are significantly lower.

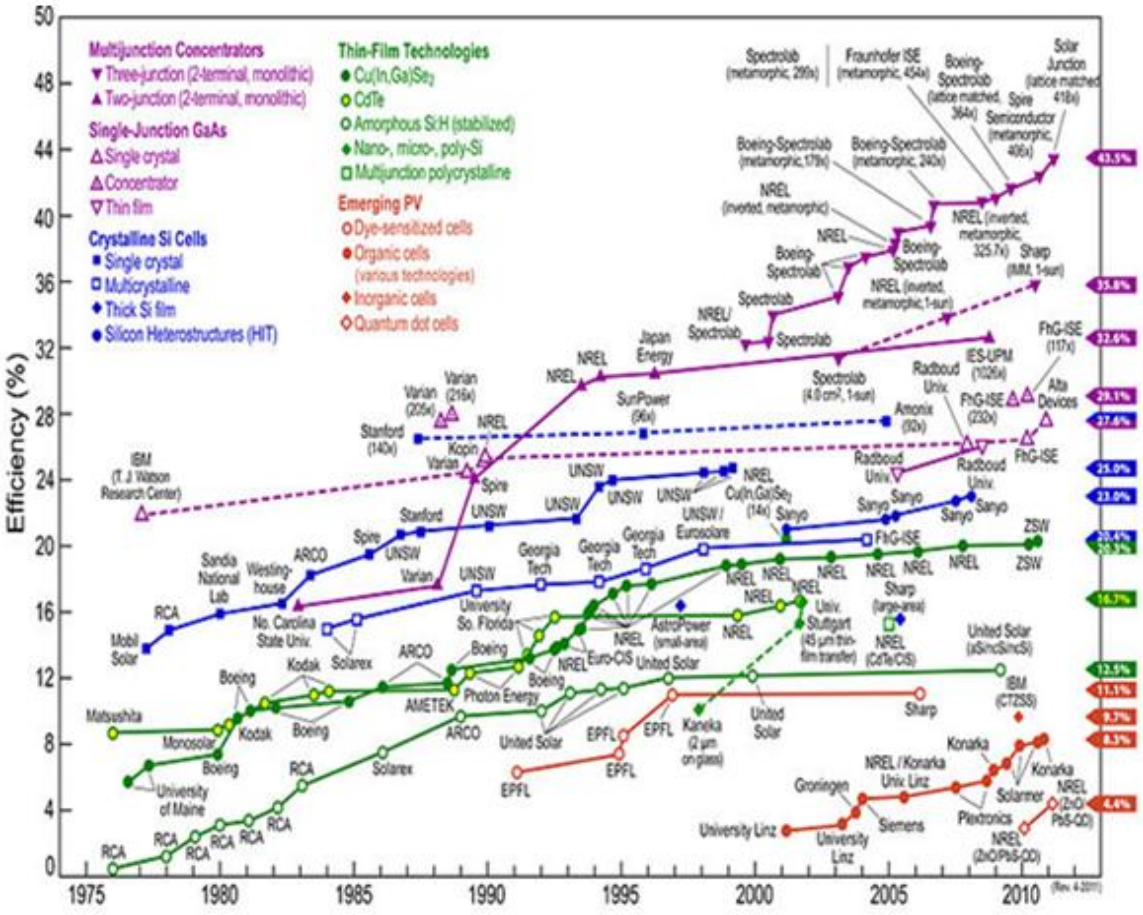

Figure 1.1.3 Best reported solar cell efficiencies [8]

To decrease the cost of solar energy, high-efficiency solar cells are of interest. Some expenses are due to the size of the power plant, thus the more efficient the solar cell is, the less size and energy production costs would be. Short circuit current (I_{sc}) and open circuit voltage (V_{oc}) are the basic parameters in evaluating the efficiencies of cells. Semiconductors with band gap between 1-1.5eV have the greatest potential to form an efficient cell (Figure 1.1.4).

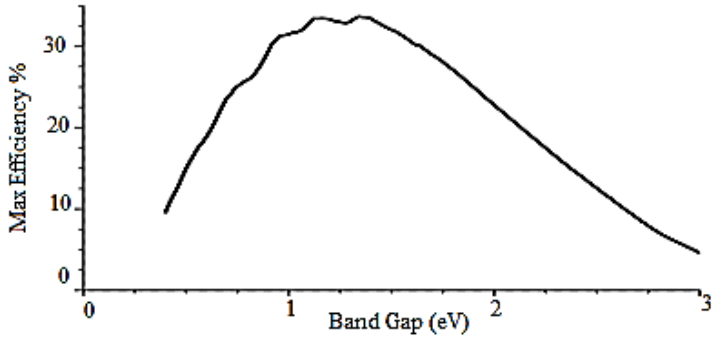

Figure 1.1.4 Band gap versus attainable theoretical solar cell efficiency [9]

The new generations of solar cells are thin film solar cells which are lower in cost and lighter in weight than the old generation, known as crystalline silicon cells. The cost of a thin film solar cell is even comparable with traditional energy sources like fossil fuels or nuclear power. In thin film solar cells, a thin film of semiconductor is deposited on any substrate such as plastic, glass, metal foils, etc. the substrate can also be either solid or flexible, and less material is used versus crystalline silicon type solar cell. There also exists more efficiency improvement potential and more cost reduction on thin film solar cells [10, 11].

In thin film solar cells, different materials can be used, and these solar cells are named based on the semiconductors which are used in their structure. Cadmium telluride solar cells [10], Copper Indium Selenide (CIS), Copper Indium Gallium di-Selenide (CIGS) [12, 13], silicon thin film solar cells, light-absorbing dye synthesized solar cell (DSSC), and organic/polymer solar cell are different types of thin film solar cells. Table 1.1.1 provides overview of the thin film solar cells and their efficiencies.

Table 1.1.1 Comparison of various thin film solar cells

Solar Cell Types	Best Efficiency	Band Gap (eV)	Characteristics
CIGS ($CuInGaSe_2$)	~ 19.5%	~ 1.1	Direct band gap, very strong light absorption
CdTe	~ 16.5%	~ 1.5	Cd is toxic if released
Amorphous Si, c-Si, nc-Si, Tandem	12-14%	~ 1.1-1.7	Not completely stable [14]
Polymer-based Solar Cells • **Dye sensitized solar cells** • **Polymer/Polymer** • **Polymer/Organic**	~11%	-	Deposited on supporting/flexible substrates
Nano Structure Solar cells • **Polymer/inorganic (nanocrystals)**	~ 6%	-	Used as quantum dots

There are several methods to deposit thin films on substrate. These methods are classified as chemical deposition and physical deposition methods. In chemical deposition, a chemical change at a solid surface caused by a solution make the deposition to take place and since the solution surrounds the solid object, deposition happens on every surface. Electroplating, chemical solution deposition (CSD), chemical vapor deposition (CVD), plasma enhanced CVD (PECVD), and Layer-by-Layer (LbL) are known as chemical deposition methods. Sputtering, pulsed laser deposition, thermal evaporator, cathodic arc deposition (arc-PVD), and electro hydrodynamic deposition (electrospray deposition) are placed in the physical deposition method category since only mechanical, electromechanical, or thermo dynamical methods are applied to produce a thin film.

Among other deposition methods, LbL offers several advantages. This method is very simple and cost effective [15]. A high degree of control over thickness can be obtained and there are varieties of material such as polymers, ceramics, metals, nanoparticles, and biological molecules, which can be deposited on different types of

rigid and flexible substrates. In this method the film is formed by deposition of alternating layers of oppositely charged materials with a washing step in between for eliminating the excess deposited materials.

1.2 Literature Review

Chalcopyrite semiconductor materials (I–III–VI_2), like CuInS/Se (CIS) and $CuInGaSe_2$ (CIGS), due to their unique optical and electrical properties, are suitable for solar cell applications and have attracted researchers' attention for several decades. CIGS solar cells have to be more cost-effective than Si-based solar cells to be able to replace them. One way is to decrease the size of the cells and make it thinner. Different deposition methods have been used so far, to deposit a thin film of CIGS. These methods are classified as vacuum and none vacuum-based processes. Co-evaporation [16, 17] and co-sputtering which are classified as vacuum-based deposition methods require extremely high vacuum and therefore are costly. In order to lower the costs, some no-vacuum methods were recently tried to replace vacuum-based deposition methods. A 13.7% efficiency CIGS thin film solar cell with bifacial configuration fabricated through three-stage growing process has been reported in [18]. The bifacial configuration includes solar cell device on both back and front contact. M. Kaelin et al. [19] reported different non-vacuum deposition methods of CIGS thin film and compared them with the vacuum methods.

Later, it has been tried to apply the nanoscale unique properties of CIGS. As reported in [20], 20 nm-sized CIGS nanoparticles were used as an absorber layer and were deposited on Mo, as the back contact, through the paste coating method. In order to improve the conductivity of the deposited film, CIS in a hydrazine-based solution was deposited on Mo-coated glass substrate through spin-coating and an efficiency of about 9% for a 0.45 cm^2 effective area was reported [21].

Recently, a 1 μm film using 7 nm-sized chloroform dispersed $CuInSe_2$ nanocrystals was deposited through LbL nanoassembly on an ITO-coated glass [22].In order to improve the current; nanocrystals were functionalized through a ligand exchange using 1, 2-ethanedithiol (EDT). After each CIS dip-coating step, EDT treatment was done to increase the nanocrystals interconnection and avoid solubility of film during subsequent dip-coating. A 16 $\mu A/cm^2$ current density at 1 V under white light illumination and 1 $\mu A/cm^2$ in the dark were obtained from the film. They claimed that EDT was acting as a CIS film modification and increased the conductivity of CIS, while CIS film itself did not have a reasonable conductivity for making a solar cell. They also used ITO as front and Al/Au as a back contact.

According to research done by Spies et al [23] and the schottky theory, in order to form an ohmic contact between a metal and a p-type semiconductor, the work function of the metal should be higher than the semiconductor. Otherwise, a schottky contact would be formed at the junction interface. The p-type CIS used in Kergommeaux's research had a work function of 4.44 eV, ITO (work function ~4.7 eV)/CIS made an ohmic, and AL (work function ~4.3 eV)/CIS a schottky contact.

In our case, since CIGS is used with a work function of 5.46 eV. According to schottky theory and research done by [23] and [24], a metal with higher work function is needed to be able to form an ohmic contact, since most of the metals have less work function than CIGS. Thus there is an unavoidable schottky barrier at both the back and front contact. But in this research it was tried to reduce the schottky barrier from at least one side.

1.3 Purpose and Scope of this Thesis

The purpose of this thesis research is to develop thin CIGS films using layer by layer nanoassembly process for solar cell application. LbL nanoassembly is readily scalable into commercial manufacturing and is also a very cost effective process. On the

other hand, CIGS is a direct band gap semiconductor with the best absorption coefficient among the other semiconductor materials, thus applying a very thin film of this material can provide a comparable efficiency to the other solar cells. In addition, unique properties of nano-sized CIGS such as more surface/volume ratio and stronger bonding to the substrate make it an attractive semiconductor material for the solar cell application. Combining these material properties with the cost effective layer by layer provide a higher energy output per unit cost. The estimated cost of LbL solar cell is compared with thin film and flexible silicon based and commercially available CIGS based solar cells costs in Table 1.3.1. The cost of LbL solar cell was estimated by considering that the bulk cost of materials will be half of the current cost purchased for laboratory use. The materials cost was estimated to be $\$20/m^2$ and the fabrication and packaging costs are estimated to be $\$10/m^2$ and $\$5/m^2$ [25], respectively. The power output of the LbL solar cell is calculated based on expected 10% solar cell efficiency, which is equal to efficiency of current thin film CIGS solar cells.

Table 1.3.1 Comparing the estimated cost of LBL CIGS solar cell with thin film Si solar cell and commercially available CIGS solar cell

	Weight (Kg) /m^2	**Power (W) /m^2**	**\$ Cost/ m^2**	**\$ Cost/ Power(W)**
Thin Film Si Solar Cell	3.26	62	221	3.5
Commercial CIGS Solar Cell	1.18	38	526	13.8
LbL CIGS solar cell	< 1.18	38	35	0.92

In this research thesis, CIGS nanoparticles were synthesized through the colloidal precipitation in an organic solvent and functionalized using PSS to reverse the surface charge and disperse in water uniformly. Nanoparticles then characterized by size and charge to further use in the film fabrication, through the LbL nanoassembly. They were also functionalized through changing the pH of the solution to disperse in water. Various LbL films of functionalized CIGS nanoparticles and polymers were then characterized by

their thickness using QCM and AFM and their I/V were measured under the light illumination using the Keithley measurement instrument for the light effect observation in order to choose the best of the films for the fabrication of solar cell.

Several solar cells were fabricated using CIGS nanoparticles (absorber layer) and different n-type semiconductor materials such as n-ZnO and CdS with the use of PEDOT and ITO as back contact. Various deposition methods such as spin-coating, drop-casting, chemical bath deposition and LbL were applied for the layers deposition. The solar cells then were tested and characterized using the Keithley measurement instrument. In addition to CIGS nanoparticles, CdS and ZnO nanopowders were also functionalized to disperse in water and characterized by size and charge for the LbL purposes. Their LbL films were also characterized by thickness using QCM and AFM.

2 PHOTOVOLTAIC EFFECT AND SOLAR CELLS

2.1 Semiconductor Materials

Semiconductor materials can have a crystalline or an amorphous structure. Crystalline semiconductor materials have been widely used in solar cell applications until now, but in recent years the amorphous semiconductors have gained more popularity due to their better intermediate conductivity, as well as quick change in conductivity with the temperature gradient. Such materials do not have the rigid structure of crystalline semiconductors like silicon; therefore, they are generally used in thin film structures, since there is no need of high electronic quality of the material and they are less sensitive to radiation damage and structural impurities. In addition to silicon, three other elements have also been used recently in commercial solar cells; germanium, silicon carbide, and gallium arsenide.

Semiconductors are often called "intrinsic" when they are pure, but their conductivity and electronic properties can be controlled by adding a small amount of other elements which are called "dopant." These impurities specify the semiconductors to be either an n or p-type. There are various discrete energy levels around the atomic nuclei of materials called "energy bands." Electrons tend to fill up the bands with lower energy, which are closer to the nucleolus first. They then start filling the next band up to a certain energy band called "valence." Unlike metals, in semiconductors and insulators, the valence band is almost filled with electrons. The electrons need to be on the conduction band, which is above the valence, to be able to flow through the material. Under certain conditions, very few (semiconductors) or none (insulator) of the electrons can move to the conduction band. These conditions are related to the energy difference between the

valence and the conduction band, called “band gap.” The band gap in semiconductors is less than 4 eV. By providing the band gap energy, electrons can be exited to the conduction band and leave holes behind in the valence. Both electrons in the conduction and holes in the valence band contribute to the conductivity in semiconductor material.

2.2 Semiconductor Junctions and Built-in Potential

Semiconductors can be doped to n or p-type based on the doping material. For example, when silicon is doped with sulfur, excess electrons are created, and the semiconductor is called as n-type. In n-type semiconductors, electron represents the majority carrier. P-type semiconductors (eg. Silicon doped with boron) have more holes than electrons. When an n-type semiconductor is brought in contact with a p-type semiconductor, a p-n junction is formed (Figure 2.2.1). When the n and p-type semiconductors come together and form a junction (Figure 2.2.1 (a)), carriers start diffusing from region of higher concentration to that of lower concentration. Since the concentration of electrons is higher on n-side and the concentration of holes is higher on p-side, electrons diffuse to p-side creating positive ions and holes diffuse to n-side creating negative ions. The created ions on the both side result in an electric field at the junction. The diffusion of carriers and recombination occurs until equilibrium is reached where further carrier recombination is prevented by the built in electric field. The built-in potential and electrical fields are shown in Figure 2.2.1 .

A diode junction can also be made through the formation of a junction between a metal and a semiconductor, called “Schottky junction” [26, 27]. In 1883, one of the first schottky solar cells was made by Charles Fritts when he was coating selenium with a thin layer of gold. Similar to p-n junctions, a depletion region is formed at the metal and semiconductor interface. For this case, the internal built-in potential is called “schottky barrier” and its magnitude is called “schottky barrier height” (SBH).

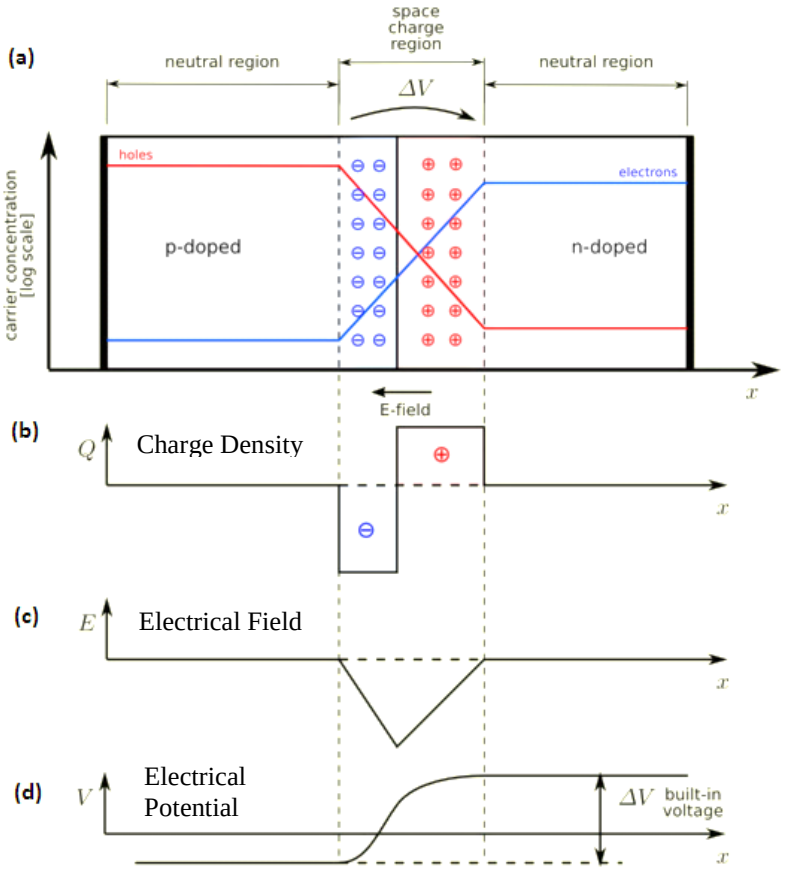

Figure 2.2.1 Schematic of a p-n junction (a), showing charge density (b), electrical fie (c), and built-in potential across the depletion region [28]

In an ideal Schottky-Mott model, the schottky barrier height can be defined in terms of the band gap of the semiconductor; work function of metal, Φ_M; the work function of semiconductor, Φ_S; and the electron affinity of the semiconductor, χ_s.

Figure 2.2.2 shows the energy band diagram and schottky barrier formation of a metal and a p-type semiconductor while $\Phi_M < \Phi_S$. As illustrated by the right going arrow in Figure 2.2.2, when metal and semiconductor are brought together and the two Fermi levels align, at thermal equilibrium, a Fermi-level-mediated charge transfer would occur; therefore, electrons move from the metal to the semiconductor. This charge transfer causes a macroscopic di-pole at the interface which is called a built-in potential, V_{BI}. V_{BI} is a potential barrier which prevents the hole at the top of the valance band of the semiconductor to go into the metal. As this charge transfer continues, V_{BI} and a

corresponding vacuum level, E_{LVAC}, arise and a potential barrier called schottky barrier height, Φ_{BP}, is also formed.

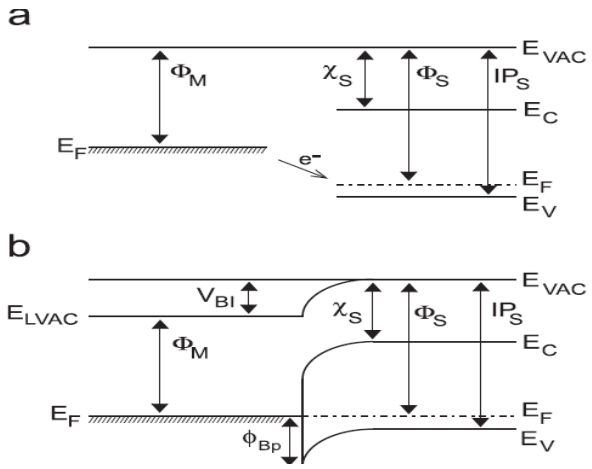

Figure 2.2.2 Energy band diagram of schottky junction between a metal and a p-type semiconductor ($\Phi_M < \Phi_S$), ideal case. (a) Materials in isolation and (b) in contact [23]

The ideal SBH for p and n-type semiconductors are given by equations (2.1 and (2.2, respectively, where E_g is called the energy band gap.

$$\Phi_{BP} = E_g + \chi_s - \Phi_S \tag{2.1}$$

$$\Phi_{BP} = \Phi_S - \chi_s \tag{2.2}$$

For non-ideal case, the charge neutrality level, E_{CNL}, of the semiconductor also is being considered. The charge neutrality level plays the role of an effective Fermi level for the semiconductor and it strongly pins the Fermi level at the metal and semiconductor interface. For a schottky junction, E_{CNL} is an intrinsic semiconductor property at the interface and can be estimated from the valance band offset data or from band structure calculations.

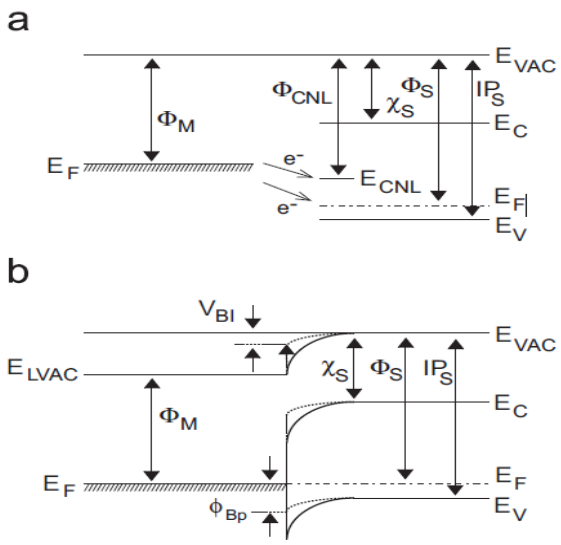

Figure 2.2.3 Energy band diagram of schottky junction between a metal and a p-type semiconductor ($\Phi_m < \Phi_s$) and ($\Phi_m < E_{CNL}$), non-ideal case. (a) Materials in isolation and (b) in contact

As shown in Figure 2.2.3, for the non-ideal case, additional charge transfer occurs at the interface. The position of charge neutrality level, E_{CNL}, relative to the metal Fermi level, E_F, determines the direction of the non-ideal charge transfer. In Figure 2.2.3 (a), the metal Fermi level is above the E_{CNL}. Therefore the charge transfers from metal causes a discontinuity in the local vacuum level, E_{LVAC} as shown in Figure 2.2.3 (b). Due to the formation of positive di-poles, the schottky barrier height (Φ_{BP}) and built-in potential (V_{BI}) are decreased.

In the schottky junction, the majority carriers (electrons) move between the metal and semiconductor creating a current called majority-carrier current ($I_{0,\ majority}$). In this case, electrons from metal have sufficient energy to pass across the barrier height at the junction interface. This current is constant at a certain applied voltage, since the barrier height between the metal and semiconductor is constant. Although this current is reverse to the current of the forward bias, it can be balanced by the majority carriers of the forward current which are excited thermally at the schottky.

In some cases, an insulating layer is applied between the metal and semiconductor in order to decrease the saturation current. High saturation current has bad effects on the performance of the solar cell and reduces the solar cell efficiency by forming extra current path of majority-carriers ($I_{0,\ majority}$). The insulating layer of few nanometers width can reduce the $I_{0,\ majority}$, while the short circuit current is not reduced much. The formation of short circuit current is due to tunneling of the minority carriers through the insulating layer. The electric field makes the minority carriers to move to the barrier and be collected to a certain degree until they are able to tunnel through the insulator layer.

On the other hand, the majority carriers are being moved away the by electric field from the junction interface. Thus, the net flow is being reduced when the majority carrier passage is slowing [8]". This junction type is called metal-insulator-semiconductor (MIS). It has been shown that the SBH of an MIS is larger than that of a metal-semiconductor (MS) structure. In the MIS systems, since there are two interface-states, and two internal electrical fields, the diode equation cannot be applied. However, by applying some ideality factors, the saturation current can be calculated as the sum of minority and majority-carrier current.

2.3 Photovoltaic Effect

Light travels in packages of energy called photons. When a semiconductor is illuminated by light, the energy of the photons is absorbed by the semiconductor. This energy can excite the electrons, which are located in the valence band. The electrons in the valence band are tightly bonded to the neighboring atoms by a covalent bond and are not able to move far from their place. When the electrons in the valence band absorb enough energy (greater than the band gap), they can be excited and move into the conduction band, where they are free to move. At this time, the covalent bond in the valence band has fewer electrons. The lack of an electron in the valence band is known as a "hole". The presence of any hole in the covalent bond causes the electrons from neighboring atoms to move into the "hole". This movement again leaves a hole behind in

the neighboring atom and causes the hole to move through the semiconductor. These photons can create movable electron-hole pairs in the semiconductor lattice which forms an electrical current. This phenomenon is called as photovoltaic (PV) effect. If the photon energy absorbed by an electron is greater than the band gap, the difference between the absorbed energy and the band gap energy is converted into lattice vibrate rather than into electrical energy .

A solar cell uses the electron-hole pair created in the depletion region of a p-n junction. When an incoming photon creates an electron-hole pair in the depletion region, the built-in electric field sweeps electron to n-region and hole to p-region. The separated electron-hole pair then travels through an external circuit for recombination, contributing to the electrical current. In Figure 2.3.1, a schematic of the photovoltaic effect is shown.

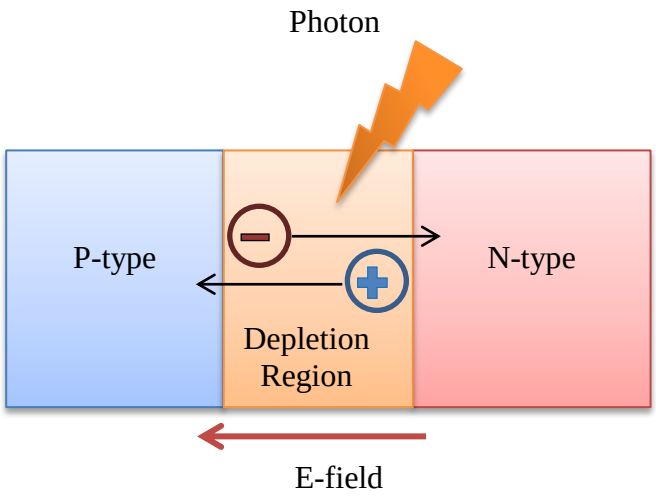

Figure 2.3.1 Schematic showing the flow of photon-generated electron and hole in the space charge region of a p-n junction.

In Figure 2.3.2 the band diagram of a simple p-n junction is shown. Photons absorbed in the depletion region create extra electron-hole pairs where electrons move toward n-side and holes move toward the p-side. The photogenerated current (I_L) direction is shown in the Figure 2.3.2.

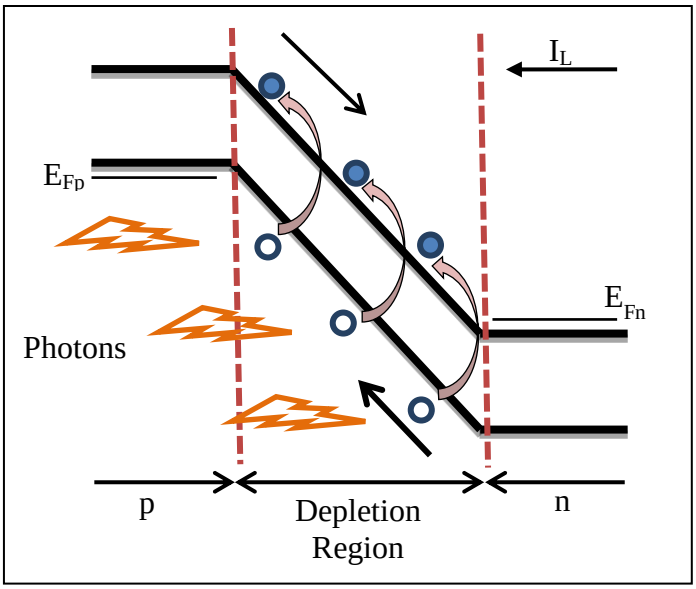

Figure 2.3.2 Schematic of a p-n junction band diagram showing depletion region and photogeneration. (the filled and unfilled circles represent electrons and holes, respectively)

2.4 Thin Film Solar Cells

Almost all of the inorganic semiconductor materials have a PV-effect, but only some of them are suitable for commercial solar cell applications, due to cost availability and efficiency reasons. The semiconductors with a direct band gap of about 1.5 eV and a high optical absorption of about 10^5/cm are consider as suitable absorber materials for the solar cell application.

The optimum thickness of a semiconductor varies inversely with the absorption coefficient, thus high absorption coefficient material results in thinner solar cells. Due to the cost and manufacturing process, the simplest semiconductors to be used in solar cells are elemental materials; however, there are none of them available with direct band gap. In addition, the closest band gap energy of elemental materials to the ideal band gap of 1.5 eV is for Si with 1.1 eV band gap and a film thickness of 50 mm should be used, at least. Therefore using the elemental materials is not an ideal case for the solar cell applications. Recently, semiconductor materials of two or more-component alloy films

are used in addition to the elemental materials in order to fulfill the solar cells requirements. For example, alloy film of a-Si:H is used which is very easy to dope, and has a large band gap and optical absorption coefficient. Other two-component (binary) materials which can be used for thin film solar cells are GaAs, CdTe, InP, etc. which are ideal, but due to the high cost, they are not applicable commercially. Increasing the number of components in the alloy film, like I–III–VI semiconductor materials ($CuIn_{(1-x)}Ga_xSe_2$), can improve the geometrical property and photovoltaic effect of the semiconductor which leads to apply a thinner film but on the other side, the phase diagram of these materials become more complex and fuzzy. In Figure 2.4.1 and Figure 2.4.2, the schematic of $Cu(InGa)Se_2$/CdS, CdTe/CdS and triple junction p-i-n a-Si:H solar cell devices are shown, respectively.

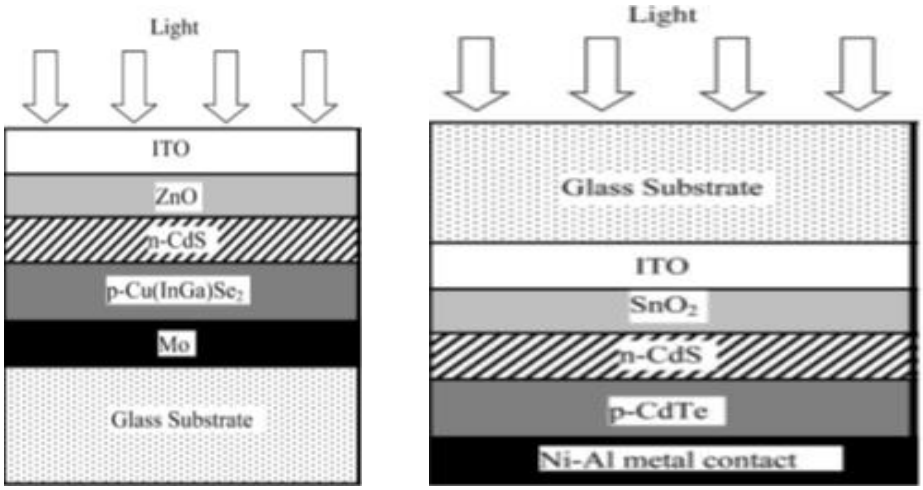

(a) (b)

Figure 2.4.1 Schematic of a (a) CIGS and (b) CdTe thin film solar cells [11]

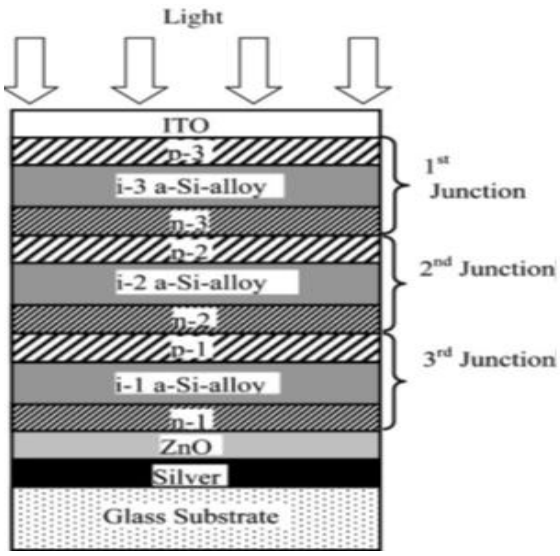

Figure 2.4.2 Schematic of a Si thin film solar cell [11]

In Table 2.4.1 the characteristics of different types of thin film solar cells are compared for different active areas. As shown, $CuInGaSe_2$ have a higher efficiency (19.2%) than a-si (12.7%) for a smaller active area.

Table 2.4.1 Best performances of various thin film solar cells [29]

Small area	Efficiency (%)	Area (cm^2)	V_{oc} (V)	J_{sc} (mA/cm^2)	Fill factor (%)
GaAs	23·3 ± 0·7	4·00	1·011	27·6	83·8
a-Si	12·7 ± 0·4	1	0·887	19·4	74·1
Si (thin film transfer)	16 ± 0·4	4·017	0·645	32·8	78·2
Si (nanocrystalline)	10·1 ± 0·2	1·199	0·539	24·4	76·6
$CuInS_2$	11·4 ± 0·4	0·511	0·729	21·83	71·7
$CuInSe_2$	15·4		0·515	41·2	72·6
$CuInGaSe_2$	19·2	0·408	0·689	35·71	78·12
$CuInAlS_2$	16·9	0·47	0·621	36·0	75·5
CdTe	16·5	1·032	0·845	25·9	75·5
GaInP/GaAs	30·3	4·0	2·488	14·22	85·6
GaAs/CIS	25·8 ± 1·3	4·0			
a-Si/CIGS	14·6 ± 0·7	2·4			
GaInP/GaAs/Ge	31·0 ± 1·5	0·2496	2·548	14·11	86·2
a-Si/a-SiGe/a-SiGe	13·5 ± 0·7	0·27(da)	2·375	7·72	74·4

Furthermore, organic semiconductor materials can be an alternative to be used in solar cells. These materials are interesting due to their excellent mechanical properties which are similar to plastic/polymer materials [30] in addition to their good optoelectrical

properties. Due to high band gap of higher than 2 eV in organic materials, only about 30% of the light can be absorbed. But they can be used at room temperature and can be deposited through very cheap processes, like spin or blade-coating, on any flexible or solid substrate. Although the efficiency of the PV devices, in which the organic semiconductors were used, are still low, but they may be suitable for disposable solar cells for small power generations.

2.5 Nanoparticle-based Solar Cells

Nanoparticle-based solar cells have become increasingly popular due the fact that their properties can be tailored at the nanoscale, which allows higher efficiency and lower cost. In general, the theory of operation of thin nanoparticle-based solar cells is similar to the bulk material solar cells. However due the fact that the active layer is made of smaller particles put together induces new phenomena in their performance. Nanoparticles have been used to utilize in new fabrication processes, such as printing and spraying, as well as in some cases to harvest new properties of the material observed at their nanometer range.

According to the discussion in the Section 2.4 about the suitable materials for thin film solar cells, the I–III–VI chalcopyrite semiconductor materials ($CuIn_{(1-x)}Ga_xS/Se_2$) have unique properties among other semiconductor materials. As an example, $CuInSe_2$ has one of the highest absorption coefficients of about $3\text{-}6\times10^5$/cm, although its band gap is about 1 eV. It also can make a very good junction with other materials. $CuInSe_2$ can also be doped to be either p or n-type according to the elemental ratios in its chemical structure, and an efficiency of about 11.4% makes it a good candidate of semiconductor materials. $CuInS_2$ with 1.53 eV band gap can also be considered as an ideal material for solar cell applications [31, 32, 33].

The other example of this type of multi-component semiconductor alloys is $Cu(InGa)Se_2$ (CIGS). By increasing in the number of components in the material

structure, the phase diagram of the material becomes very complex and hard to have a control on the composition formation during the synthesis (nanoparticles) or during the deposition (co-evaporation). Furthermore, using rare metals like In and Ga in the composition makes it more expensive; however, because of using a very thin film of only a few microns or less on a large-scale area and obtaining high efficiency as well, CIGS-based thin film solar cells come in consideration recently and could be the most cost-effective solar cells among the others. CIGS-based solar cells have also shown a very good stability at outdoor temperature and comparing to silicon solar cells, they have a very high radiation resistance and can be easily deposit on any light weight flexible substrate and solve spacing problems. Currently the best CIGS solar cell efficiency is reported to be 19.4% for 0.994 cm^2 effective area [12, 34].

3 SYNTHESIS AND FUNCTIONALIZATION OF CIGS NANOPARTICLES

CIGS ($CuIn_xGa_{(1-x)}Se_2$) has a chalcopyrite structure similar to a diamond structure shown in Figure 3.1 . This structure consists of tetragonal unit cells as shown in Figure 3.1. The value of x can vary from 1 (pure CIS) to 0 (pure CGS). Depending on the value of x, the band-gap energy (E_g) also varies from 1.0 to 1.7 eV [35, 36]. There are many parameters which have impact on the CIGS solar cell efficiency such as doping, defects, impurities, grain size, film uniformity, etc. [35]. The ratio of Ga/(Ga+In) is also very important for the solar cell performance and should be approximately 0.3 for the best solar cell performance [36, 37]. To reach p-type conductivity, CIGS should be Cu-poor and annealed under high pressure Se-vapor. But if the material is Cu-rich and Se deficit, an n-type CIGS would be formed [38].

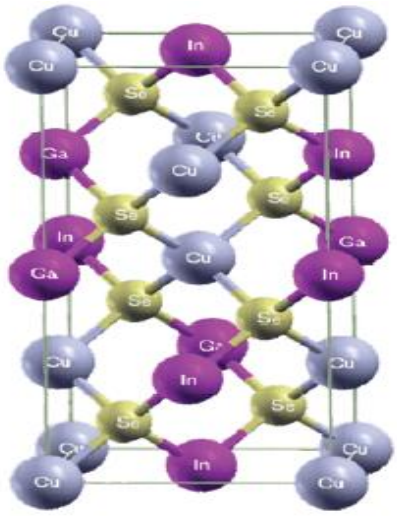

Figure 3.1 Schematic of CIGS crystal structure

3.1 Synthesis and Purification

CIGS nanoparticles were synthesized using 25 ml of oleylamine (OLA). The OLA was heated at 205˚C for 2 hours while nitrogen was bubbling in the liquid so that the oxygen was replaced with nitrogen in the liquid [39, 40, 41, 42]. Then the nitrogen was removed and the inlet was sealed to avoid oxygen going in again. After that, heating was continued at 205˚C for at least 10 hours to make the OLA turn yellow. The yellow color presence means that water has been evaporated. Then in a nitrogen-filled glove box, 10 ml of OLA was added to 0.316g of Se in a flask, Flask A. The solution in Flask A was heated at 250 ˚C for 1 hour, while being stirred with a magnet at medium speed. Meanwhile, in two other separate flasks (Flasks B and C), 5ml of OLA was mixed with 0.294 g of $InCl_3$ in flask B and 5 ml of OLA was mixed with 0.198 g CuCl. Solutions in Flask B and C were heated at 250 ˚C for 30 minutes. The flasks were stirred with magnets at medium speed. Then Flask B and C were added to Flask A and 0.118g of $GaCl_3$ was added to them. The whole mixture then was heated at 250 ˚C for 75 min. And the mixture again was stirred with magnets, but at high speed.

After completion of the synthesis, ethanol is added to the cooked mixture and sonicated for 15 minutes and centrifuged at 7000 rpm for 10 minutes. The precipitate from the centrifuge step is collected while the supernatant is discarded. Then the precipitate is dispersed in chloroform and sonicated for 15 minutes, and centrifuged at 13000 rpm and the precipitate is discarded again and excess ethanol is added. After sonication for 15 minutes the solution is centrifuged at 12000 rpm. The cleaning steps are repeated 3 more times.

The synthesized nanoparticles were characterized by size and zeta-potential using Malvern nanosizer measurement instrument. The first solution used in the LbL process was CIGS nanoparticles dispersed in an aqueous solution and the second solution was 0.1 g/ml NaOH added to the first solution to reverse the charge of the particles. Water was purified using a Millipore-Milli-Q water purification system in which ion-exchange and

filtration as well as reverse osmosis are involved. The Scanning Electron Microscopy (SEM) images of CIGS nanoparticles dispersed in water is shown in Figure 3.1.1.

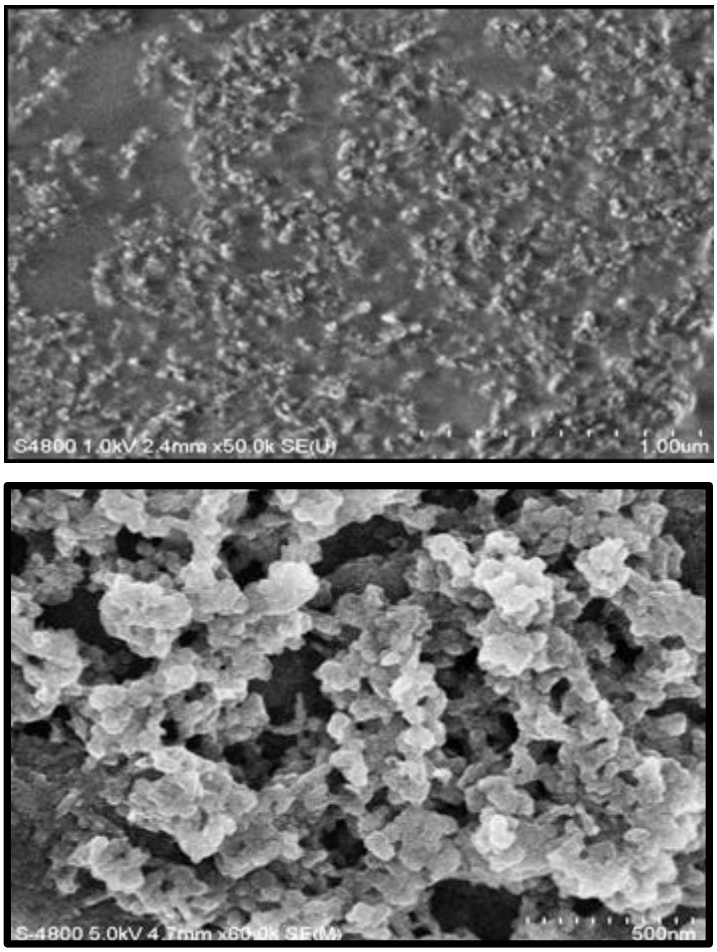

Figure 3.1.1 SEM images of CIGS nanoparticles dispersed in water

3.2 Size Distribution and Zeta Potential

Figure 3.2.1 shows the size distribution of the particles dispersed in chloroform. In Figure 3.2.1, the average and peak size of the particles has been measured to be 75 nm and 68 nm, respectively. This result is good since the particle size range is less than 100 nm which is in the nanoscale range. This result shows that the nano-sized CIGS particles are very well dispersed in chloroform and this property can be used for the purification process after the synthesis as well. By addition of chloroform to the solution of mixture

of large and small-sized particles, smaller particles are dispersed in chloroform while the larger ones are precipitated.

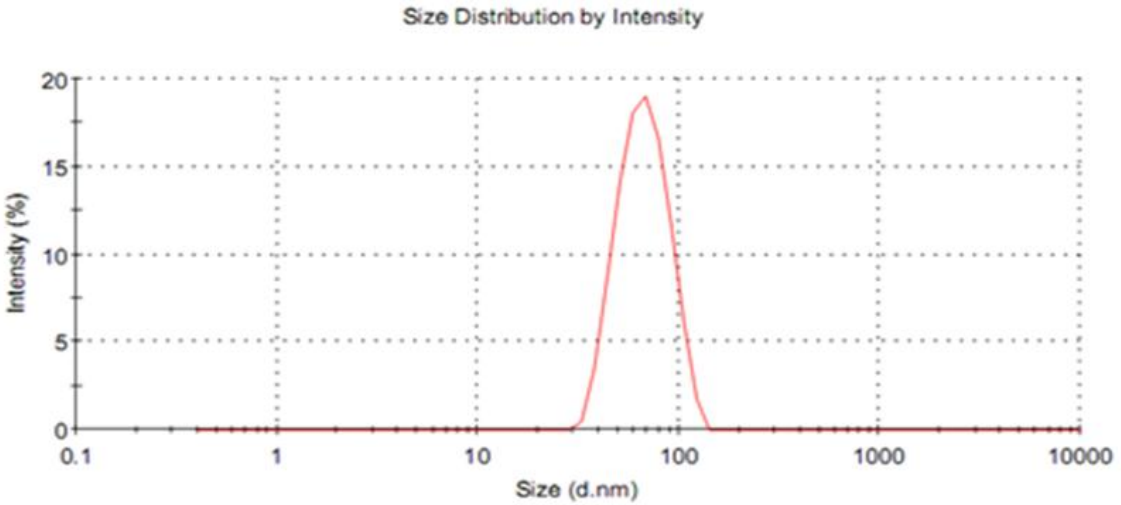

Figure 3.2.1 Size distribution of CIGS nanoparticles in chloroform

CIGS nanoparticles have positive zeta potential when they are dispersed in water (Figure 3.2.3). But in chloroform, the average zeta potential of the particles is negative (-34 mV) covering the positive zeta potential of the CIGS particles, but due to the wide zeta distribution range from -90 mV to 0 mV, chloroform cannot be a good dispersant for the LbL purpose.

In other measurement, 0.1 ml of chloroform dispersed CIGS solution was dispersed in 1 ml of ethanol. The size and zeta potential of CIGS nanoparticles in the solution are measured to be 594 nm and -19 mV, respectively. The results show that after the ethanol addition, particles were aggregated and became larger (594 nm) and started to settle down. This fact can be used for the purification process, where it is necessary to separate the CIGS nanoparticles from the unwanted supernatant. By adding the ethanol to the solution, CIGS nanoparticles are aggregated and settled down in the solution and the top part of the solution can be discarded and the precipitate be kept. When zeta potential was measured for the ethanol addition case, still a wide zeta potential range, from

negative to positive, could be seen, and although the average zeta potential of the particles was measured to be -19 mV, the solution cannot be used for the LbL purpose.

The size and zeta potential distribution of CIGS nanoparticles in water are shown in Figure 3.2.2 and Figure 3.2.3, respectively. In Figure 3.2.2, the average size and the peak was measured to be 115 nm and 27 nm, respectively. From the graph it can also be seen that most of the particles are in the range of 15-100 nm. This result was taken right after the purification. After a few days, aggregation of the particle was observed. This result indicates that for a short term period, particles can be kept in water and still have a nano range size distribution, but for a long term period, they should remain in chloroform.

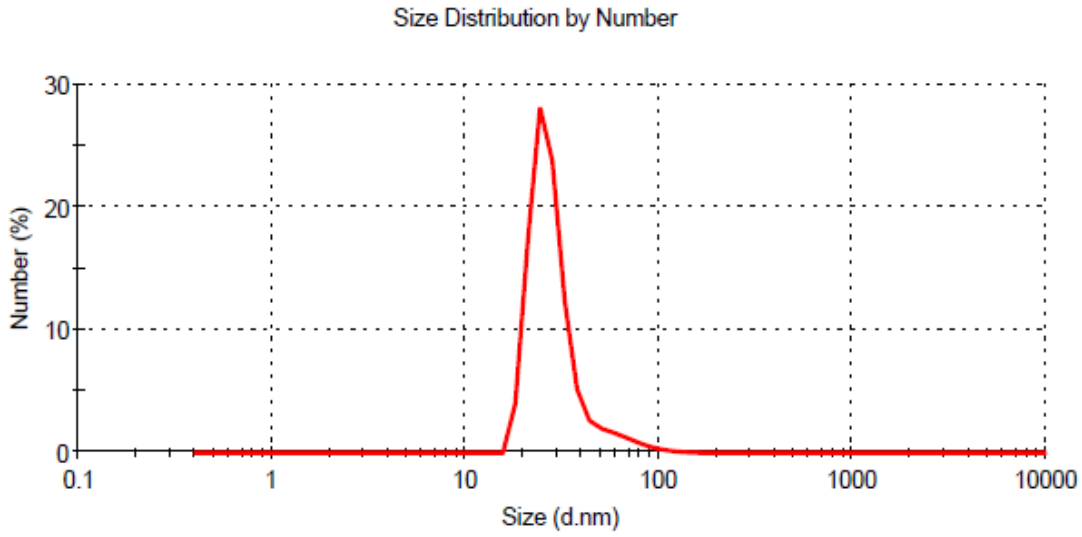

Figure 3.2.2 Size distribution of CIGS nanoparticles in water

As seen in Figure 3.2.3, the zeta potential distribution of CIGS particles in water was measured to be 61 mV. The result was taken right after the purification. Since the zeta potential distribution has a narrow single peak on the positive zeta potential range, it can be used for the LbL purpose as positive-charged nanoparticles.

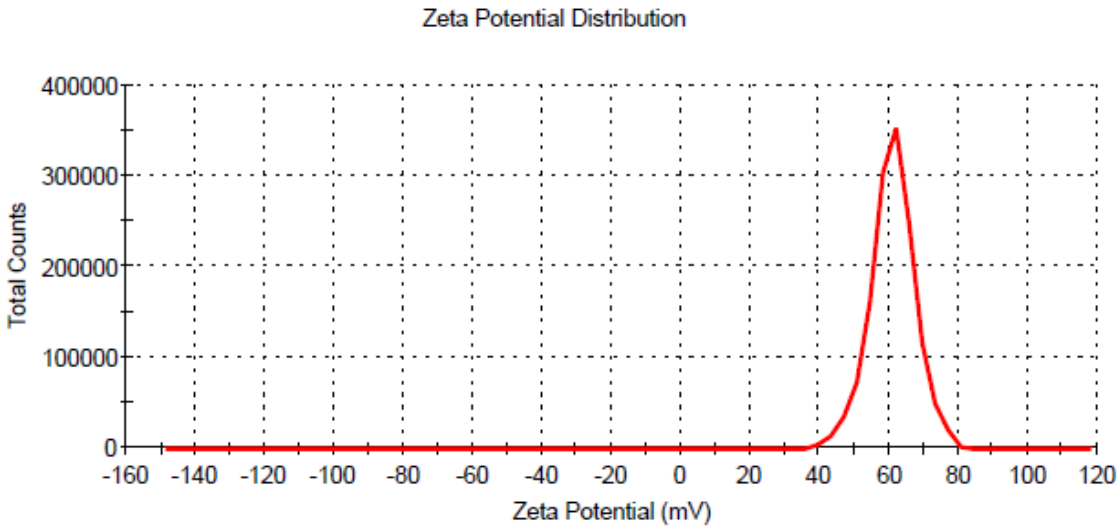

Figure 3.2.3 Zeta potential distribution of CIGS nanoparticles dispersed in water

3.3 Functionalization of Nanoparticles

CIGS surface charge modification was accomplished through a ligand exchange process with NaOH and PSS and also through physically removing the OLA from the particles through multiple washing steps. The purpose of this surface modification was to disperse the nanoparticles in the water. Figure 3.3.1 show that CIGS nanoparticles dispersed in water have +61 mV zeta potential before NaOH addition. By adding and increasing the NaOH to the aqua solution of CIGS, surface charge of particles decreases and is finally saturated at -43.4 mV, which indicates reversal of the surface charge. Figure 3.3.2 shows the zeta of CIGS nanoparticles at 10.5 pH.

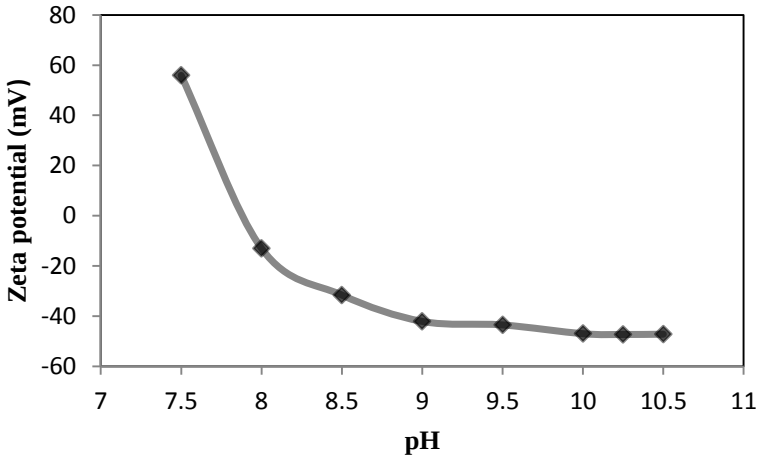

Figure 3.3.1 Zeta potential of CIGS nanoparticles vs. pH of the solution

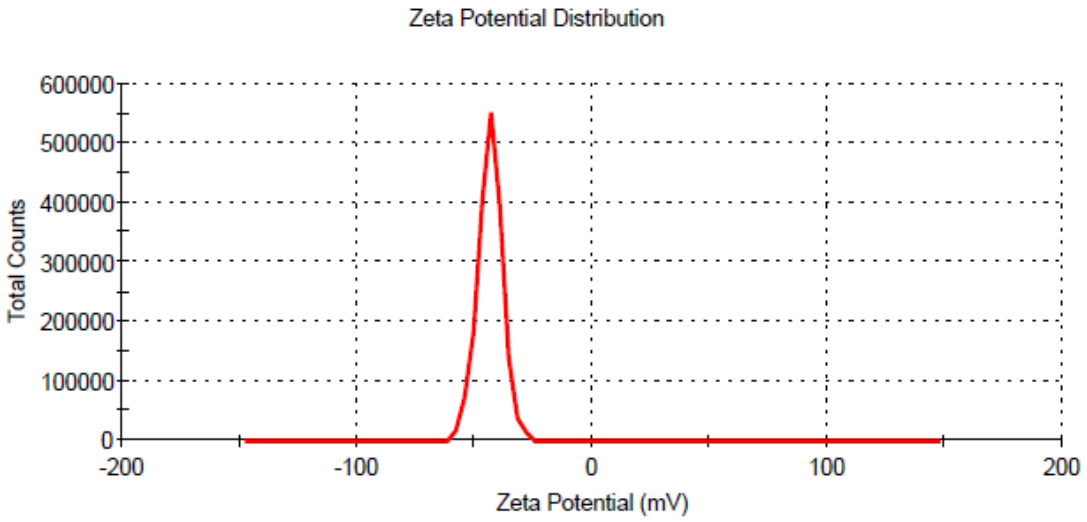

Figure 3.3.2 Zeta potential of CIGS nanoparticles in NaOH solution

The CIGS particles dispersed in water were coated with PSS for a stable dispersion and obtained good negative surface charge. Figure 3.3.3 shows the zeta potential distribution of CIGS nanoparticles coated with PSS and dispersed in water. The concentration of PSS was 30 μg/ml. As PSS was slowly added to the CIGS solution, the zeta potential of CIGS nanoparticles was slowly decreased until the zeta potential of the solution reversed. There was also an interesting observation beside the charge reversion that the size of the particles started to increase while the zeta started to decrease towards zero starting from 38 mV. This is due to the attachment of PSS on the surface of CIGS

nanoparticles, as well as due to the agglomeration of the particles. As the PSS started to make the solution negative, the particle size started to decrease. When the zeta reached -21 mV, the size of the nanoparticles reached to a point a little bit larger than the starting point with no PSS which indicates the addition of PSS, on the CIGS surface. This is due to the increased surface charge leading to a better dispersion and less agglomeration. The zeta potential of -56.9 mV was obtained for CIGS nanoparticles in a 10 mg/ml PSS solution.

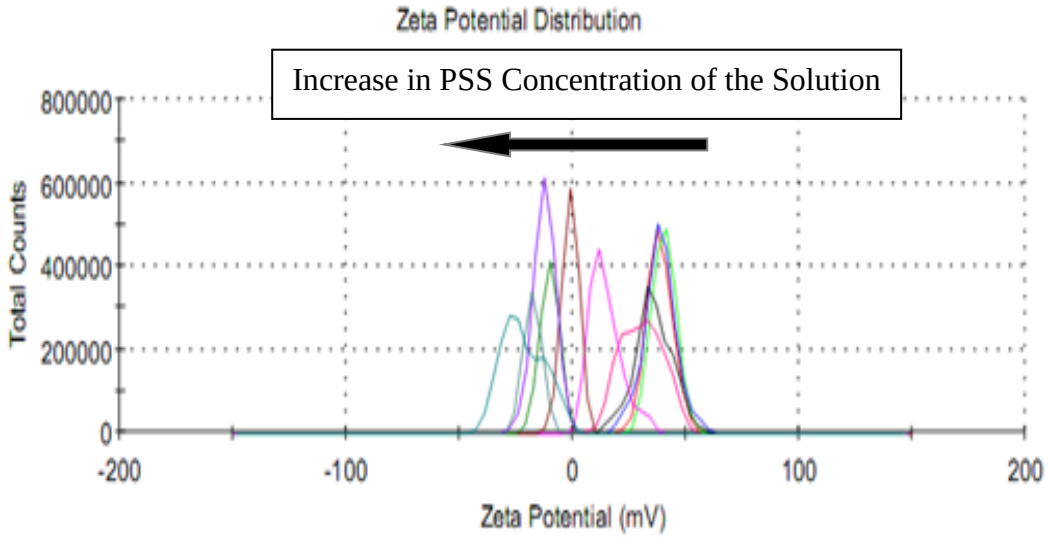

Figure 3.3.3 Showing decreasing zeta potential of CIGS nanoparticles dispersed in water with the addition of PSS

Figure 3.3.4 shows that the coating of the particles with PSS results in a more narrow size distribution which was due to the high negative surface charge that prevents the particles from coming closer, and thus prevents agglomeration.

(a)

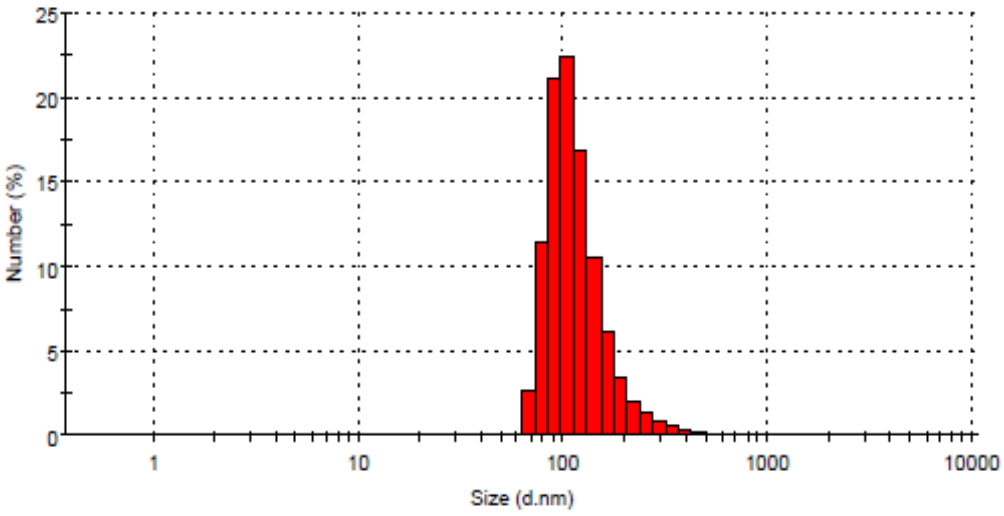

(b)

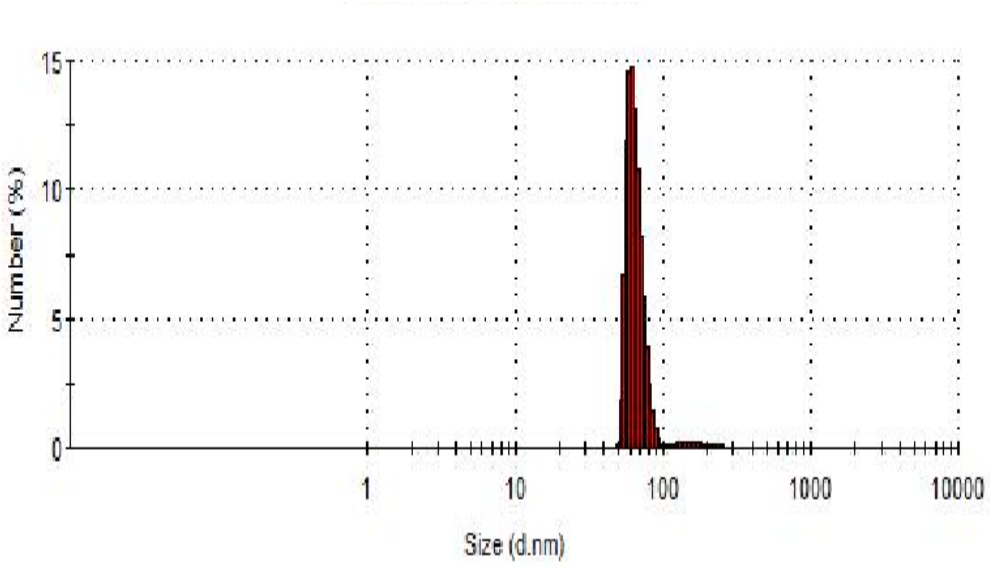

Figure 3.3.4 Size distribution of CIGS nanoparticles (a) before and (b) after dispersing in PSS solution

The SEM Image of PSS-coated CIGS nanoparticles were taken on a gold substrate. The sample was prepared by placing a drop of the solution on gold-coated

silicon substrate and dried at room temperature. The SEM image of CIGS nanoparticles in the PSS solution is presented in Figure 3.3.5. It shows that the particle size of CIGS nanoparticles after coating with PSS became larger, around 150 nm, which also confirms verifies the size measured with nanosizer.

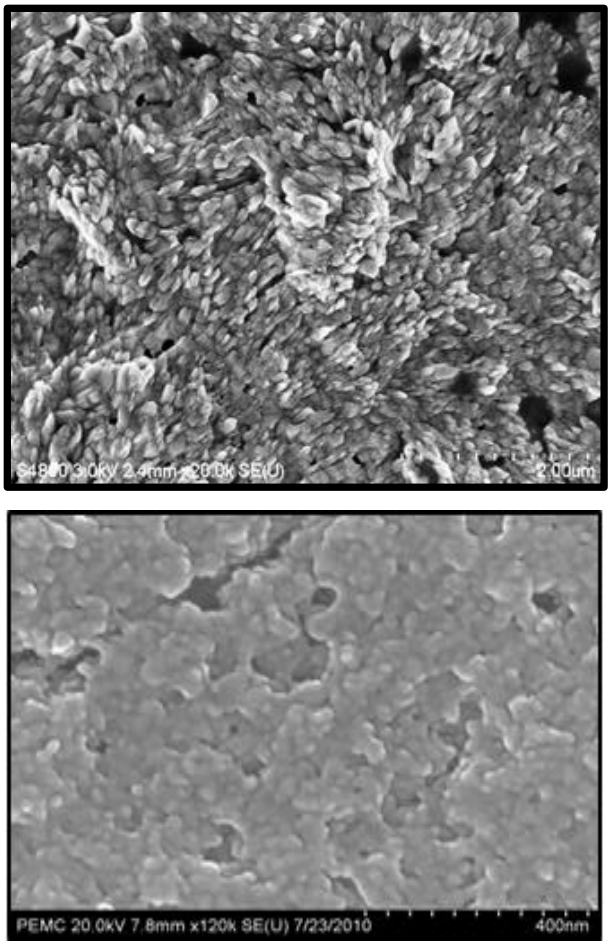

Figure 3.3.5 SEM image of CIGS-PSS nanoparticles dispersed in water

A summary of the surface charge and size of CIGS nanoparticles in different dispersant is provided in Table 3.3.1. From the table, PSS-coated CIGS has the minimum particle size, thus is the best case to be deposited through the LbL process.

Table 3.3.1 Summary of charge and size distribution

Nanoparticles	Dispersant	Surface Charge (mV)	Size (nm)
CIGS	Chloroform	–34	75
CIGS	Ethanol	–19	594
CIGS	water	+61	115
CIGS-NaOH	water	–43.4	520
CIGS-PSS	water	–56.9	60

4 LAYER-BY-LAYER ASSEMBLY OF NANOPARTICLES

4.1 Overview

Layer-by-Layer (LbL) nanoassembly is a bottom-up fabrication method which is based on sequential deposition of oppositely charged polyelectrolytes [43, 44] or nanoparticles on any rigid or flexible substrates, of different shapes and sizes [45]. The substrate usually need surface modification prior to the LbL process [46]. In order to modify the surface charge of the substrate, either chemical reaction or deposition of multi-layers of charged groups on the substrate are performed before the deposition of the actual layers. The precursor layers can be made up of polymers with net charges of (+ve) or (–ve) called polyions (polyanions or polycations). A schematic of the LbL process is shown in Figure 4.1.1.

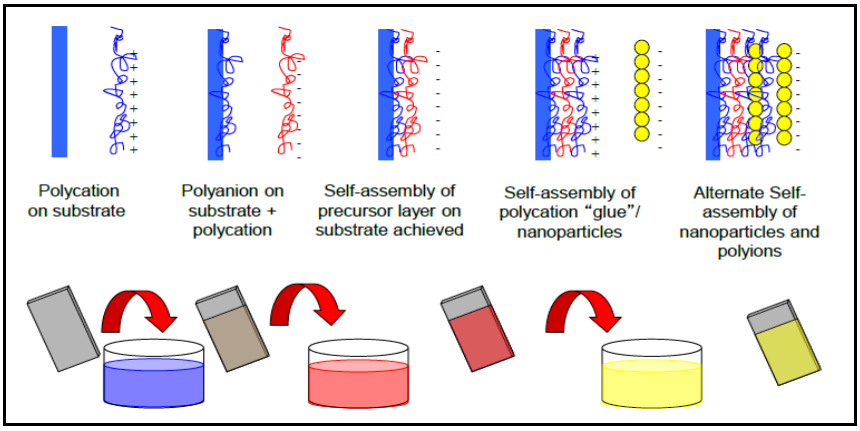

Figure 4.1.1 Schematic showing the layer by layer (LbL) nanoassembly process through alternate adsorption of polycations and polyanions [43]

In LbL methods, film thickness range of 1-1000 nm can be obtained, and although the process is slow, the fabricated film has fewer defects or cracks compared to drop-

casting or spin-coating [47]. The driving forces between the oppositely charged nanoparticles or polyelectrolytes are electrostatic forces. LbL nanoassembly is a low cost and precise fabrication technique which provides a highly uniform and thermal stable film. The film obtained by this method is hard to dissolve in organic solvents, and also a wide variety of charged polymers and nanoparticles as well as substrate selections can be applied in the LbL process.

The film thickness fabricated through LbL nanoassembly process can be measured using Quartz Crystal Microbalance (QCM) instrument. To measure the film thickness, the LbL process performed on the QCM as the substrate. The resonant frequency of the QCM changes with the mass change of the deposited materials, Figure 4.1.2 shows the schematic of an LbL process on a QCM instrument.

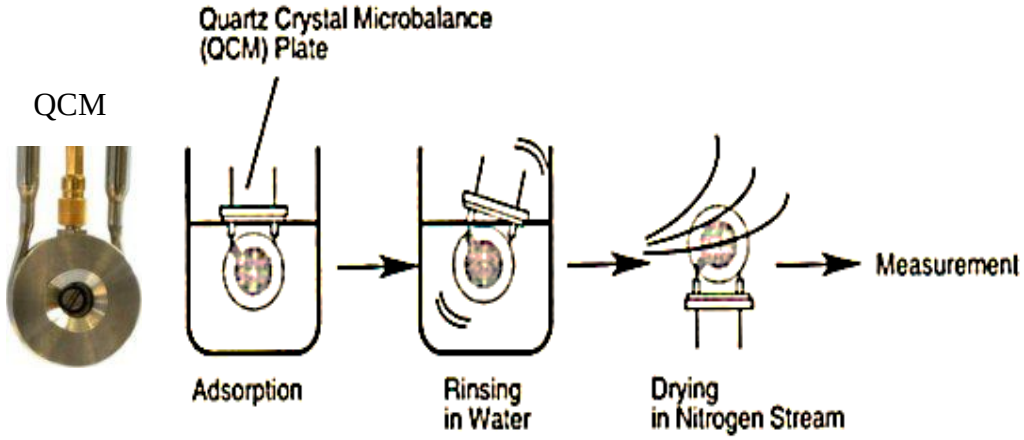

Figure 4.1.2 Showing the LbL process on a QCM measurement instrument [48]

Equations 4.1, 4.2 and 4.3 are used to measure the film thickness using frequency change of the QCM. Since the change in the frequency value of the QCM is read from the device, from Equation 4.1, Δm can be found and then using Equation 4.3, thickness of the film is measured.

$$\Delta f = \frac{2f0\text{^}2}{\sqrt{(\rho q)(\mu q)}}\frac{\Delta M}{A} \tag{4.1}$$

$$f_0 = \frac{C}{d} \tag{4.2}$$

$$Thickness = \left(\frac{\Delta M}{A}\right)\left(\frac{1}{\rho \mathrm{f}}\right) \tag{4.3}$$

The parameters are defined in Table 4.1.1. The density (ρ), Shea modulus (μ), and the wave speed (C) for an AT-cut quartz crystal are 2.648 g/cm^3, 2.947×10 ^{10} Nm^{-2} and 3336 ms^{-2}, respectively.

Table 4.1.1 Parameter definitions used in equations

Parameter Definitions	**Symbols**
Resonant Frequency (Hz)	f_0
Frequency Change (Hz)	Δf
Mass Change (g)	Δm
Piezoelectrically Active Crystal Area (Area Between Electrodes, m^2)	A
Density of quartz	ρ
Shea Modulus Quartz for AT-Cut Crystal	μ
Wave Speed for Quartz	C
Thickness of the Quartz	d

LbL nanoassembly gives a practical and versatile opportunity on surface modifications [45]. There are also a wide range of applications in the fabrication of sensors, biosensors and electronics using the LbL nanoassembly method.

4.2 CIGS Nanoparticles Film

The layer-by-layer depositions of CIGS nanoparticles dispersed in water have been performed. The two oppositely charged aqueous CIGS solution, as described in Section 3.3, were used in the LbL process. The film was deposited on a Quartz Crystal Microbalance (QCM) to measure the film thickness and study the film build up

characteristics by alternate dipping in the charged solutions for 5 minutes. Each layer deposition was followed by a 5 minutes water washing step (CIGS/wash/CIGS/wash).

Figure 4.2.1 shows the QCM results for 4 bi-layers of CIGS (positive) and CIGS dispersed in NaOH (negative), plotted as change in frequency (dashed line) and film thickness (solid line) against the number of layers deposited. Increase in film thickness after each layer deposition is shown. From the figure, the average thickness of the total thickness after 4 bi-layers is 18 nm.

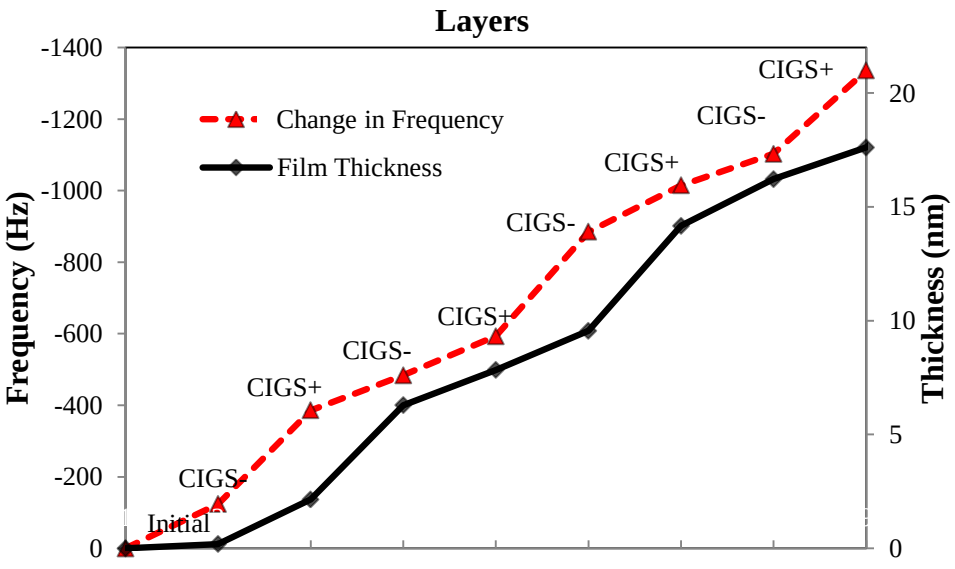

Figure 4.2.1 QCM Frequency change vs. film thickness after each layer deposition

Atomic Force Microscopy (AFM) profiling was conducted on a CIGS sample with 4 bi-layers. To be able to see the film thickness, a scratch was made on the film using the AFM probe tip. As shown in Figure 4.2.2, the film thickness was measured to be 15 nm.

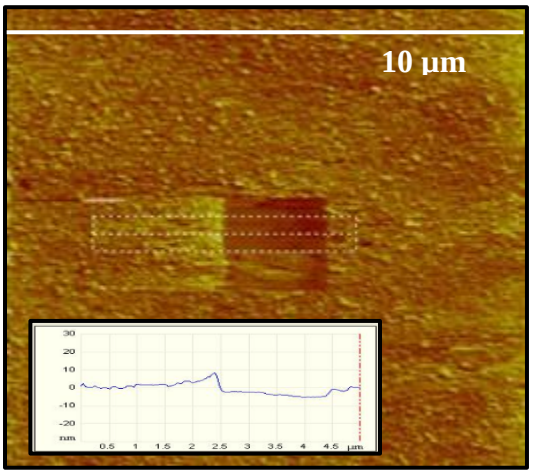

Figure 4.2.2 AFM image of 4 bi-layers of CIGS on a glass substrate

4.3 CIGS Nanoparticles and Polymer Films

CIGS nanoparticles films were also deposited with PSS and PEI polymers. In the first case, a positively charged CIGS and PSS were used for LbL deposition. In the second case, CIGS nanoparticles were coated with PSS, and they were used to deposit LbL film with PEI.

A Layer-by-layer process performed on a QCM using CIGS nanoparticles dispersed in water, which have +61 mV surface charge, and PSS, which has -56.9 mV surface charges. For making the film, 3 bi-layers of PSS/PEI as precursor layers and 4 bi-layers of CIGS/PSS as main layers were deposited. The immersion time period for each solution and also for the intermediate washing steps was 5 minutes. As shown in Figure 4.3.1, a decrease in frequency and an increase in film thickness can be seen. The film thickness is measured to be about 15 nm. In Figure 4.3.2, again the film thickness of three bilayers of PSS/PEI as precursor layers and 4 bi-layers of PSS/CIGS as main layers are shown but the immersion time periods were 20 minutes and 10 minutes for the precursor (PSS/PEI) and main (CIGS/PSS) bi-layers, respectively. Each layer was then followed by a 10-minutes washing step. In this case, a film thickness of about 24 nm was achieved. Comparing the film thickness in Figure 4.3.1, Figure 4.3.2 clearly shows that

an increase in the immersion time period causes more uniform and thicker film to be created. Figure 4.3.1presents the frequency change of precursor and main deposited layers for different immersion time period. A larger decrease in the frequency for both precursor and main layer was obtained for the longer immersion time (10 and 20 minutes).

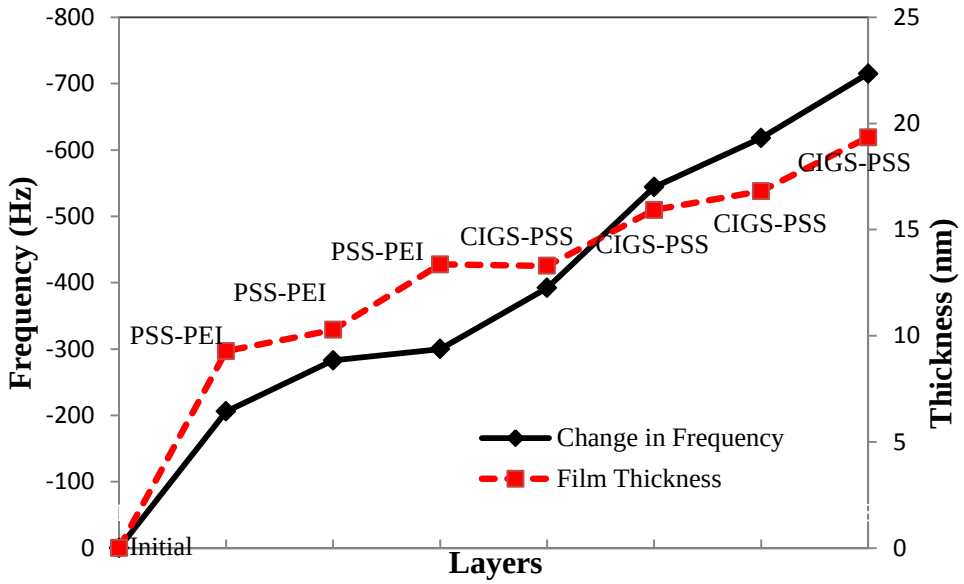

Figure 4.3.1 Frequency and thickness changes for three deposited bi-layers of PSS/PEI as precursor layers and 4 bi-layers of CIGS/PSS

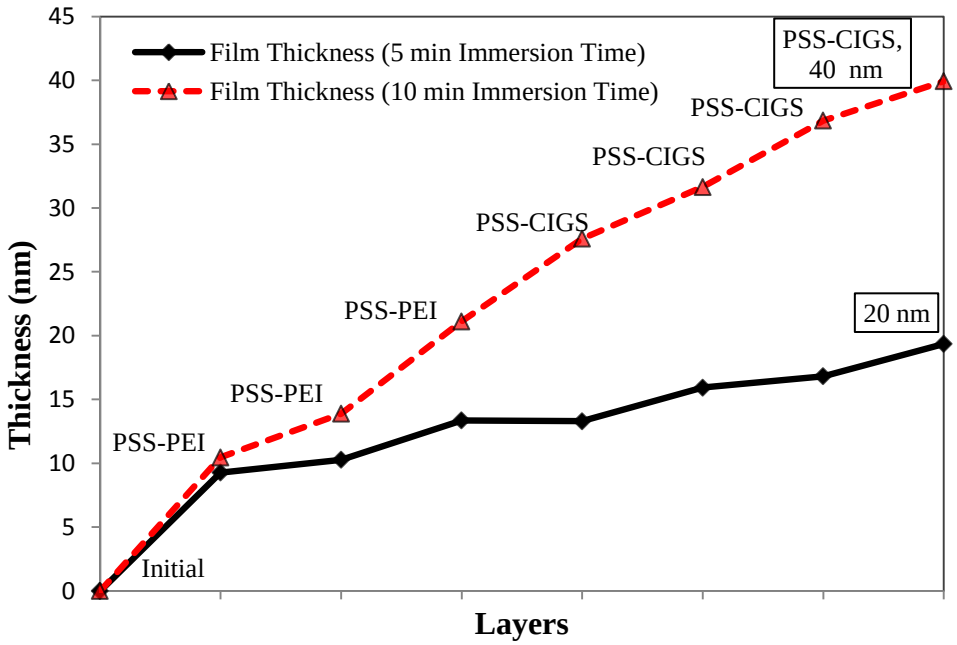

Figure 4.3.2 Showing a comparison of film thickness of 3 bi-layers of PSS/PEI as precursor layers and 4 bi-layers of CIGS/PSS as main layers for different immersion times

Table 4.3.1 Comparision of change in frequency measured for different immersion times as indicated in the table

	Dashed Line	**Solid Line**
	4 bilayers of CIGS/PSS for 5 min +3 precursor layers for 5 minutes	4 bilayers of CIGS/PSS for 10 min +3 precursor layers for 20 minutes
Total Δf for precursor layers(Hz)	-300	-280
Total Δf for main deposited layers(Hz)	-534	-939

The CIGS nanoparticles were coated with PSS for more stable dispersion and to form a better LBL film. In order to prepare the CIGS-PSS solution, for the LbL process, 50 µl of CIGS dispersed in isopropyl alcohol (IPA) was added to 6.25 mg/ml water dispersed polystyrene sulfonate (PSS). The concentration of polyethyleneimine (PEI) was 3mg/ml. The LbL process was done on ITO-coated glass substrate. The substrate was

dispersed in each CIGS-PSS/PEI solution for 5min in a way that the top layer was the CIGS film.

Figure 4.3.3 shows the QCM results of 4 LbL bi-layers of PSS-coated CIGS and PEI, in which the frequency decreased with the addition of each layer. On the same graph the thickness of the total film, after each layer deposition is demonstrated. From the figure, the total thickness of the film after 4 bi-layers is 35 nm.

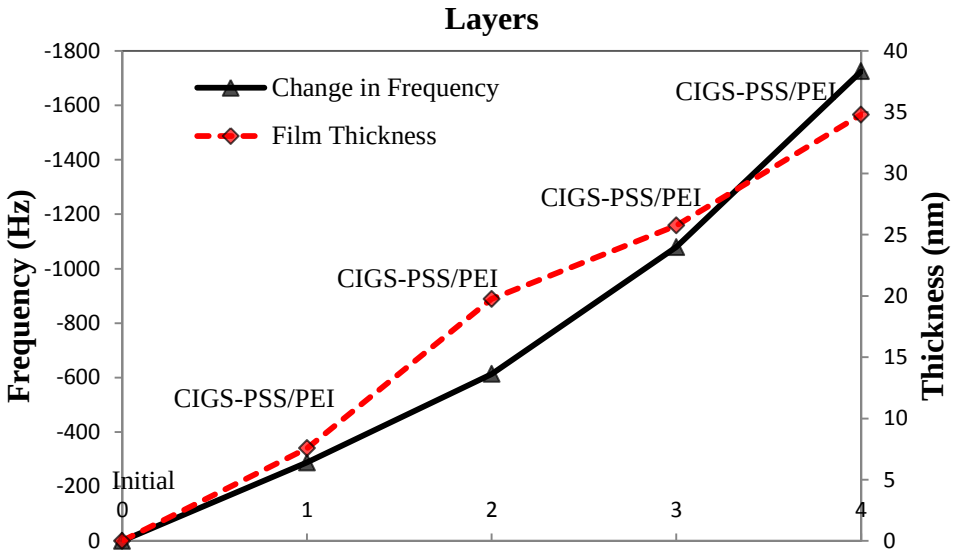

Figure 4.3.3 QCM Frequency changes as well as film thickness after deposition of each PSS-coated CIGS and PEI bi-layer

Figure 4.3.4 shows digital images of films taken using a digital camera through the microscope with 5/0.12 magnification. A film of 7 layers of CIGS-PSS/PEI on ITO substrate is shown in Figure 4.3.4 (a) and a film of 13 layers of CIGS-PSS/PEI is shown in Figure 4.3.4 (b) which also shows the scratch mark using micro-manipulator probes.

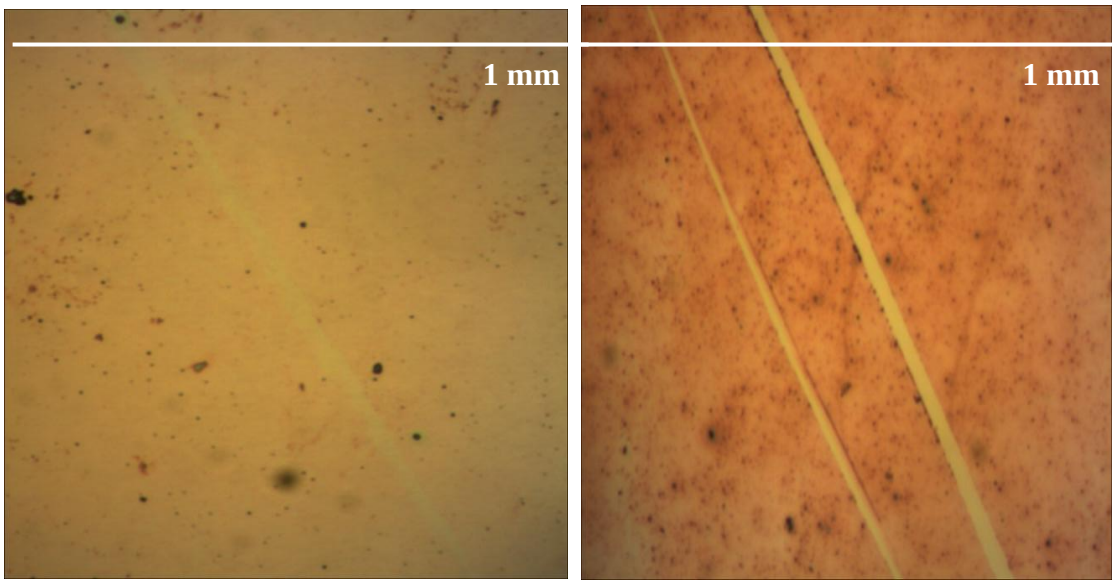

(a) (b)

Figure 4.3.4 The Image of a CIGS film taken by Keithley for (a) 7 and (b) 13 layers on ITO

The AFM images of the films were taken and the results are presented in Figure 4.3.5. As shown in Figure 29. SEM image of a 13-layer film of PSS-coated CIGS and PEI on an ITO glass substrate is shown in Figure 4.3.6. The sample was prepared by LbL of the substrate in each of the solutions for 5 min. A 5-minute washing step was used between each of the deposition steps.

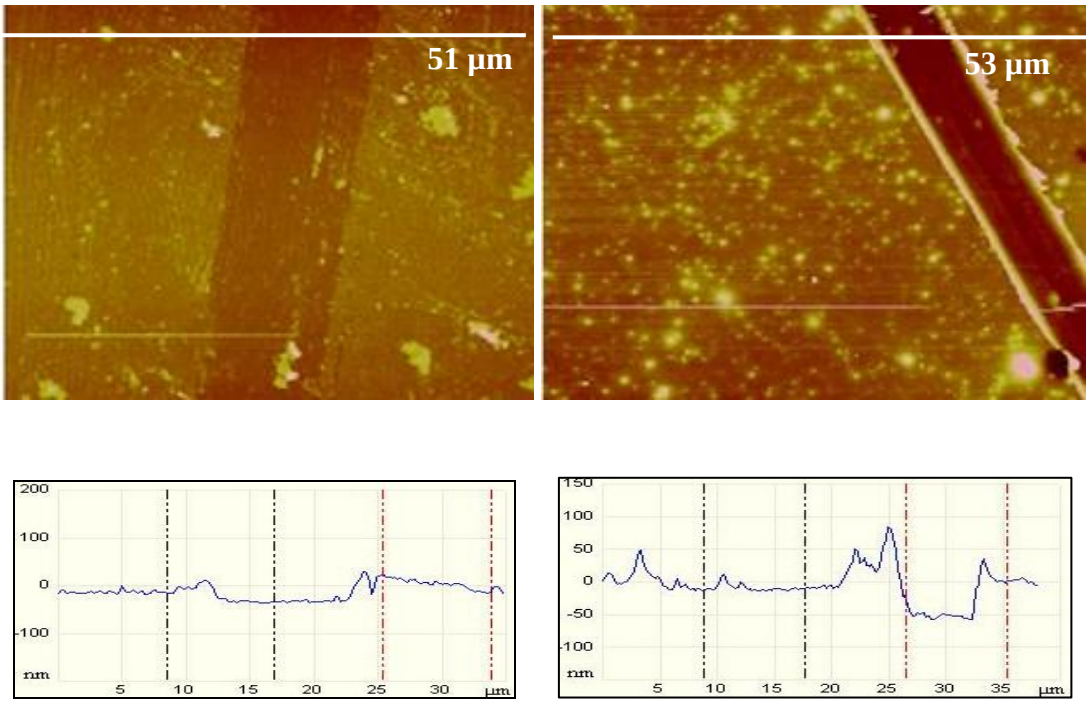

(a) (b)

Figure 4.3.5 AFM image of the CIGS film for (a) 7 and (b) 13 layers on ITO

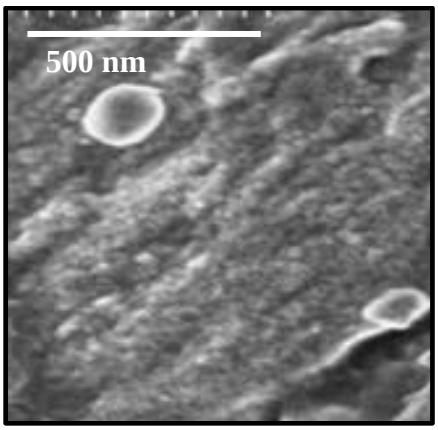

Figure 4.3.6 SEM image of 13 layers of PSS-coated CIGS and PEI film

4.4 ZnO, CdS, and Polymer Films

The layer-by-layer nanoassembly was also performed using zinc oxide (ZnO) and PEI to form a thin film of ZnO on an ITO-coated glass substrate. ZnO particles were

coated with PSS to disperse in water. To prepare the ZnO solution for the LbL application, 0.03 g of 6% Al-doped ZnO nanopowder was added to the 6.25 mg/ml PSS aqua solution. The concentration of 3 mg/ml was used for the PEI aqua solution. The LbL process has been done similar to Section 4.2 on an ITO-coated glass. In Figure 4.4.1, the size distribution of ZnO in the PSS solution is shown to be mostly in the range of 40-60 nm. The Zeta potential of ZnO in the PSS solution was measured to be –57.5 mV and that of PEI was +16 mV.

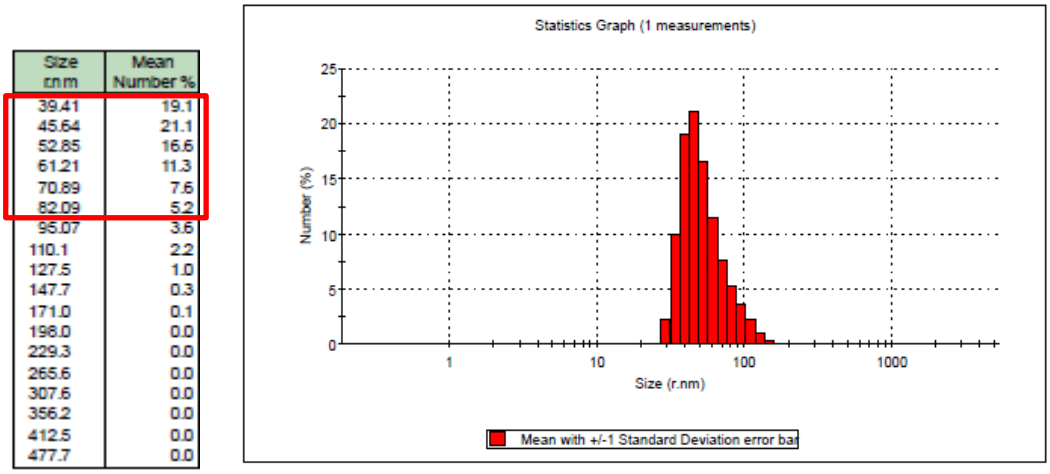

Figure 4.4.1 Size distribution of ZnO nanoparticles in PSS solution

Figure 4.4.2 shows the QCM results of 5 LbL bi-layers done using ZnO-PSS and PEI, in which the frequency is decreased while the number of layers increased. On the same graph the thickness of the total film, after each layer deposition is demonstrated. From the figure, the total thickness of the film after 5 layers is 67 nm.

.

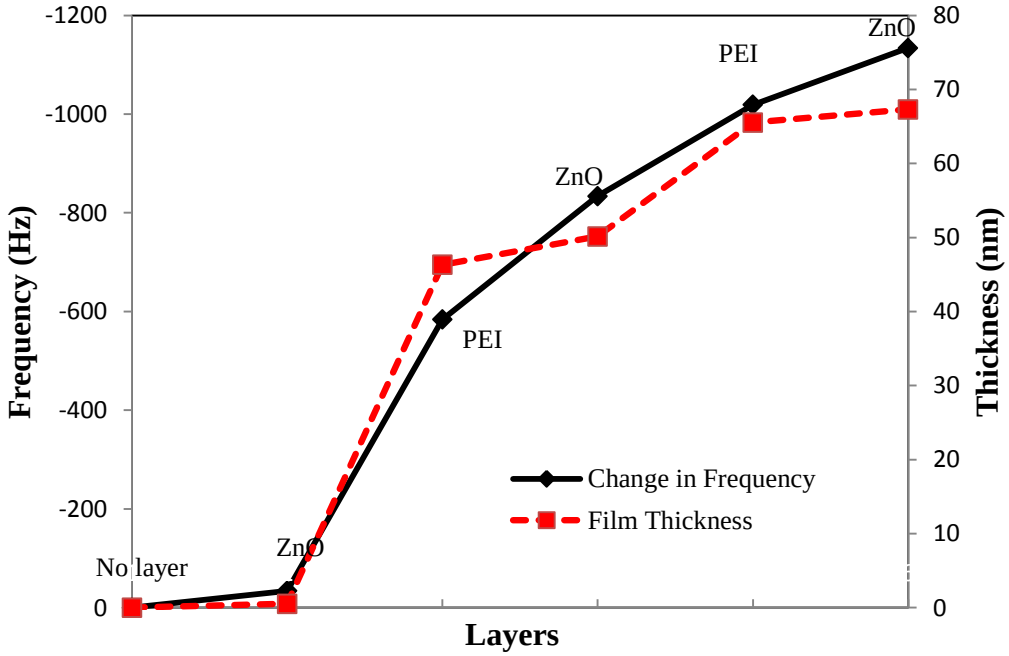

Figure 4.4.2 Frequency vs. film thickness of a 5 layer ZnO-PSS and PEI film

Figure 4.4.3 shows the digital images of 7 and 13 layers of ZnO-PSS/PEI film which was taken with a microscope with and the scratches were made by Keithley micromanipulator probes. It can be seen that a uniform film of ZnO is formed on the ITO-coated glass using the LbL process. The AFM image of the film is presented in Figure 4.4.4. As shown in the figure, the film thickness is about 80 nm. For this LbL process, the ZnO particles average sizes were mostly measured to be in a range of 40-60 nm (Figure 4.4.1). But there were some smaller particles of size 30-40 nm as well, which could be deposited.

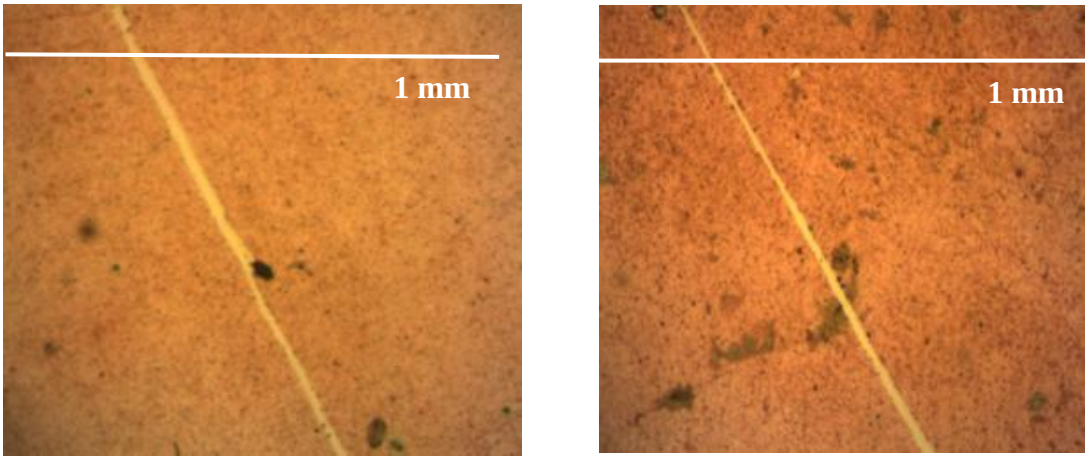

(a) (b)

Figure 4.4.3 The image of a ZnO-PSS and PEI film taken by Keithley for (a) 5 and (b) 10 layers on ITO

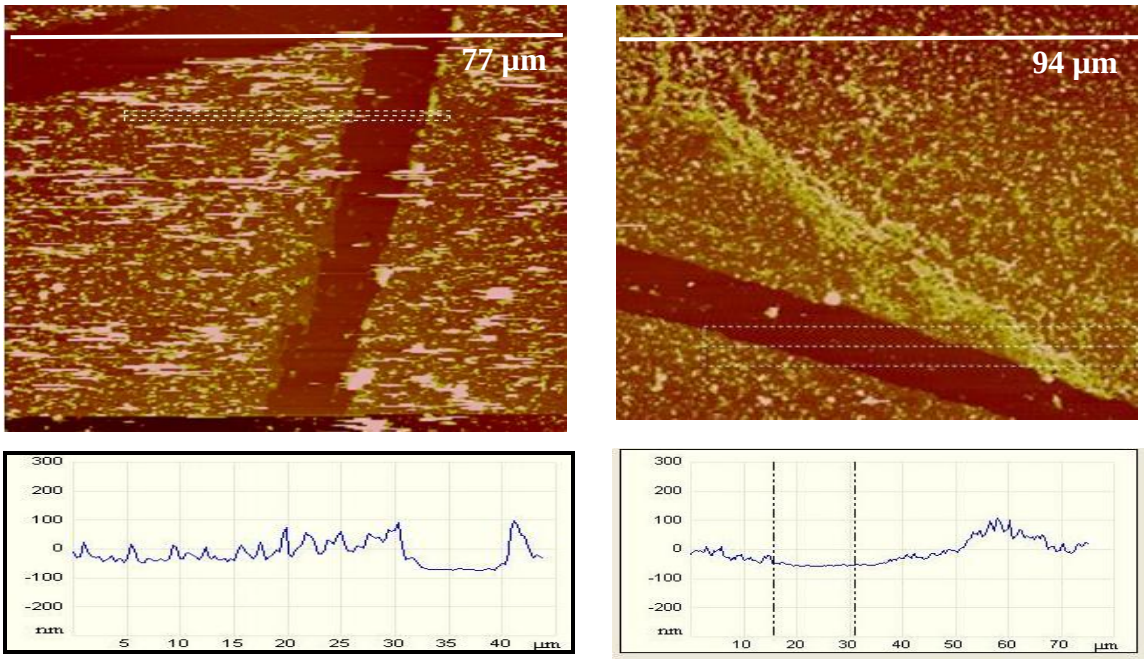

(a) (b)

Figure 4.4.4 AFM image of the ZnO-PSS and PEI film for (a) 5 and (b) 10 layers on ITO

In further experiments, the LbL process was done using PSS-coated cadmium sulfide (CdS) and PEI. CdS was coated again with PSS to disperse in water and then was

deposited on an ITO-coated substrate. The CdS solution for the LbL process was made using 0.05 g CdS nanopowder added to 3 ml of Toluene and sonicated. Half of this CdS/Toluene solution was then added to 6.25 mg/ml water-based PSS solution and sonicated again until a uniform mixture of the solution was obtained. Then, the solution was kept steady till particles were precipitated. The dispersant was then taken from the bottom for the LbL process. The concentration of PEI was 3 mg/ml. Zeta potential of CdS in the PSS solution was measured to be –74.6 mV and that of PEI was 16 mV. The LbL process has been done similar to Section 4.2. As shown in Figure 4.4.5, the size distribution range of CdS nanoparticles in the PSS solution is 9-18 nm.

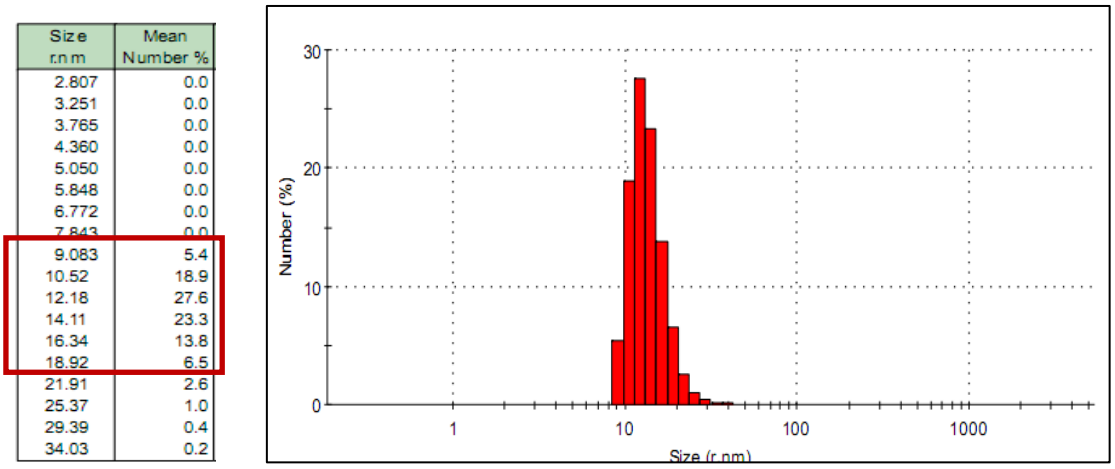

Size r.n m	Mean Number %
2.807	0.0
3.251	0.0
3.765	0.0
4.360	0.0
5.050	0.0
5.848	0.0
6.772	0.0
7.843	0.0
9.083	5.4
10.52	18.9
12.18	27.6
14.11	23.3
16.34	13.8
18.92	6.5
21.91	2.6
25.37	1.0
29.39	0.4
34.03	0.2

Figure 4.4.5 Size distribution of CdS particles in PSS solution

Figure 4.4.6 shows the QCM results of 5 LbL layers done using CdS-PSS and PEI, in which the frequency is decreased while the number of layer increased. On the same graph the thickness of the total film, after each layer deposition is demonstrated. From the figure, the total thickness of the film after 5 layers is 31 nm.

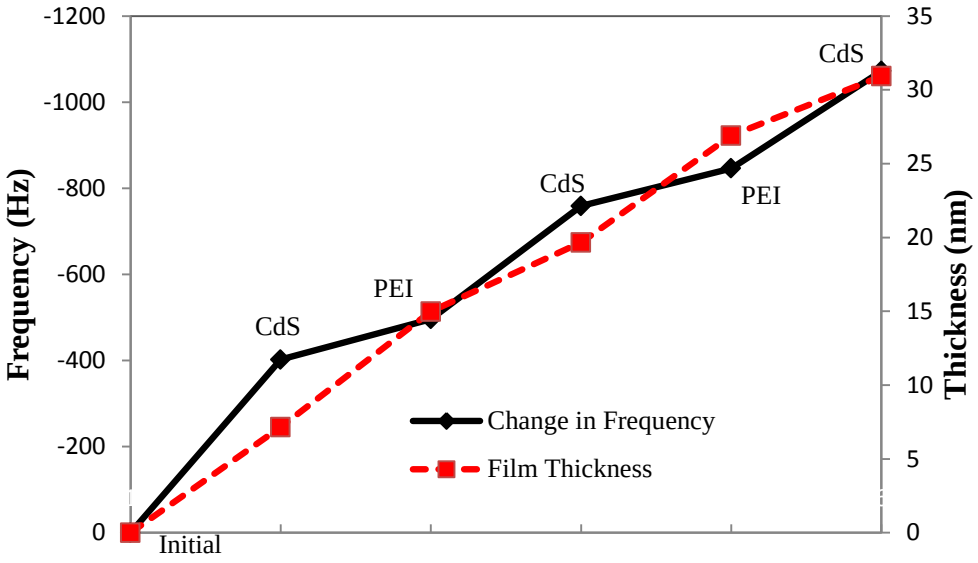

Figure 4.4.6 QCM results of the CdS/PEI LbL film

Figure 4.4.7 shows digital images of 5 and 10 layers of CdS-PSS/PEI film which were taken with a microscope with 5/0.12 magnification and the scratches were made by Keithley micromanipulator probes. It can be seen that the CdS film on the ITO-coated glass using the LbL process is not as uniform as CIGS and ZnO films. The AFM image of the film is shown in Figure 4.4.8.

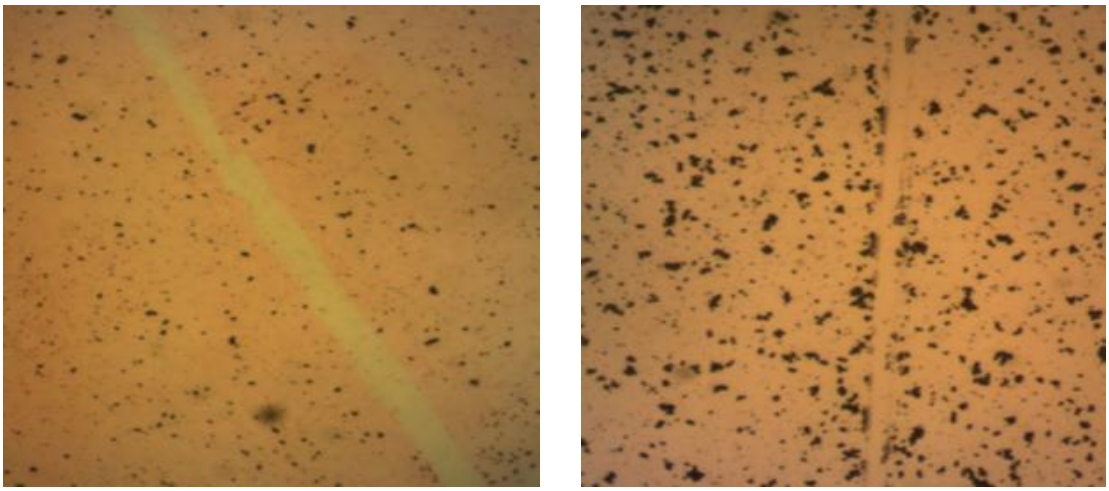

(a) (b)

Figure 4.4.7 Image of a CdS film taken by Keithley for (a) 5 and (b) 10 layers

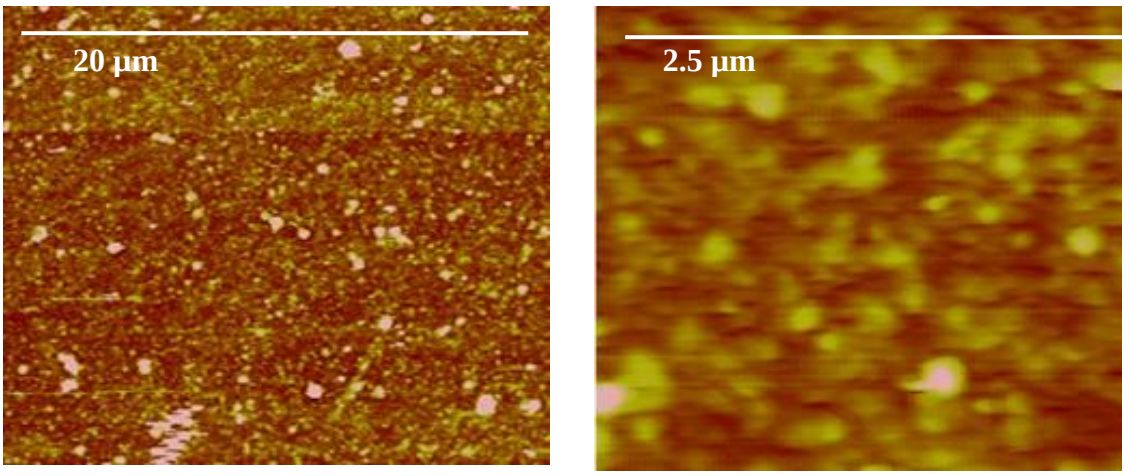

(a) (b)

Figure 4.4.8 AFM images of 5 layers of Cds on an ITO-coated substrate for (a) 20 and (b) 2.5 µm surface areas

4.5 Summary

A series of layer by layer (LbL) processes were performed through the deposition of oppositely charged groups (particles or polymers) dispersed in water. As discussed in chapter 3, CIGS nanoparticles have positive zeta potential, and the negatively charged CIGS water was obtained by raising the pH of the solution as well as by the coating with PSS. These CIGS nanoparticles, PSS and PEI were used to form various types of CIGS films through LbL nanoassembly process. The coating of CIGS nanoparticles with PSS resulted in uniform and stable water dispersion, however, small increase in the particle size was observed.

Various combination of positively and negatively charged groups (particles and polymers) dispersed in water were used to fabricate the CIGS film. The thicknesses of the LbL nanoassembly films were then measured using quartz crystal microbalance (QCM). Frequency of the quartz crystal was measured after the deposition of each layer. The thickness of 4 bi-layers of CIGS+/CIGS−, CIGS/PSS, and CIGS-PSS/PEI were measured to be 18, 20, and 35 nm, respectively. These results show that, CIGS-PSS/PEI film resulted in thicker film and it was also observed to be more uniform than the other films. It was also observed that increasing the immersion time helps to deposit more material (nanoparticles) on the substrate (thicker film) and form a more uniform film. However, the measured film thicknesses were less than expected. For example for a 4 bi-layer of CIGS-PSS/PEI film, with an average size of 60 nm CIGS nanoparticles, a total thickness of 240 nm would be expected but the actual thickness measured was only 35 nm, while the measured thickness of the film is less than the theoretically expected, it has been attributed to the fact that in the LbL nanoassembly process, the smaller nanoparticles have higher probability of attaching to the substrate than bigger particles. The reason is that, the smaller particles moves faster in a solution than bigger particles and because of higher surface/volume ratio; they carry higher surface charges per unit volume and can form a stronger bond to the substrate.

The AFM and QCM results of LbL films were compared. The thickness of the films measured using AFM was comparable to the results obtained from QCM, however, the thickness measured through AFM was little smaller than the one measured by QCM. Also, it was shown that by increasing the layers to more than 20 bi-layers, denser and thicker film could be obtained. A summary of the film thickness results of 8 layers using various CIGS nanoparticles film types is shown in

Table 4.5.1. the thickness per layer of CIGS+/CIGS- and CIGS/PSS films were almost the same but the one for CIGS-PSS/PEI is much more. That is due to the fact that PSS enhance the surface charge of the CIGS nanoparticles and causes more nanoparticles bond to the substrate. Thus thicker film would be formed.

Table 4.5.1 Summary of Thickness per Layer for each CIGS Nanoparticles LbL Film

Film Types	Surface Charge (mV)	Number of Layers	Film Thickness (nm)	Thickness / Layer
CIGS+/CIGS-	+61/-43.7	8	18	2.25
CIGS/PSS	+61/-56.9	8	20	2.5
CIGS-PSS/PEI	-56.9/+16	8	35	10.2

Furthermore, LbL nanoassembly was conducted using ZnO-PSS/PEI and CdS-PSS/PEI on a QCM. ZnO and CdS were coated with PSS to disperse in water. Each of the solutions used for the LbL process were water-based. A film thickness of 140 nm was obtained for a 5 layer ZnO-PSS/PEI LbL film while the particle size distribution of ZnO nanoparticles in the PSS solution was measured to be 40-60 nm. Also, for a 5-layer CdS-PSS/PEI film, a thickness of 31 nm was obtained while the size distribution of CdS nanoparticles in the PSS solution was measured to be 9-18 nm. Table 4.5.2 shows a summary of the film thickness results obtained using CdS and ZnO nanopowders.

Table 4.5.2 Summary of thickness per Layer for each ZnO and CdS nanopowders LbL film

Film Types	Surface Charge (mV)	Number of Layers	Film Thickness (nm)	Thickness / Layer
ZnO-PSS/PEI	-57.5/+16	5	67	13.4
CdS-PSS/PEI	-74.6/+16	5	31	6.2

5 ELECTRICAL CHARACTERIZATION

The current versus voltage (I/V) characteristics of the LbL deposited films were measured using Keithly Semiconductor Characterization Instrument (4200-SCS) and with the help of four micromanipulator probes. For all I/V characterizations, the following sample preparation method was used: First, a 500 μm channel was etched on ITO coated glasses, LbL film was deposited on the ITO substrate by alternate dipping in oppositely charged dispersions of respective materials including washing steps after each dip-coating, and the samples were air dried.

5.1 CIGS Nanoparticles Film

Positively and negatively charged dispersions of CIGS nanoparticles (obtained through pH control, as discussed in Section 3.3, were used to deposit 6 bi-layers of LbL CIGS/CIGS film on a 500 μm etched channel on an ITO-coated glass. The immersion time for each of the solutions was 5 minutes followed by a 5-minute intermediate water washing step. The sample was air dried afterwards and the I/V characteristics were measured, first in the dark (no-light), and then under light illumination (all lights on). Then, 4 additional bi-layers of CIGS were deposited making a total of 10 bi-layers and the measurement for I/V was repeated. The results for both 6 and 10 bi-layers are shown in Figure 5.1.1. The increase in conductivity (decrease in resistivity) clearly indicates the photoelectric effect in the film, and as expected a 10 bi-layer film has a lower resistivity than a 6 bi-layer film. Figure 5.1.2 shows the I/V characteristics of 25 layers of CIGS/CIGS LbL film. The results show that the fabricated CIGS film has a resistivity of

5.5 MΩ.m and when exposed to light, decrease in resistivity by 87% and increase in current was observed.

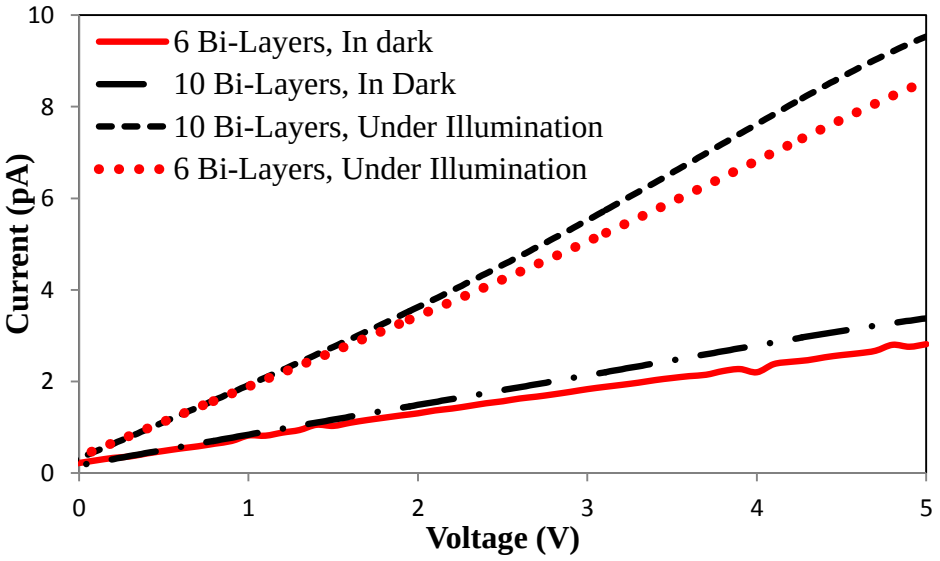

Figure 5.1.1 The I/V characteristics of 12 and 20 layers of CIGS films showing photovoltaic effect

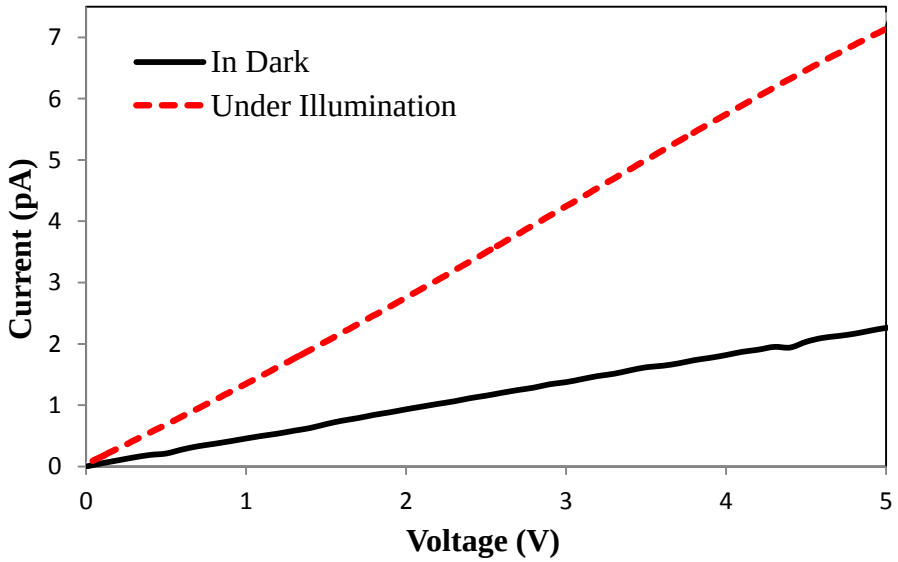

Figure 5.1.2 The I/V characteristic of a 25-layer CIGS LbL film with and without the presence of light, showing the decrease in resistivity by 87%

5.2 CIGS Nanoparticles and Polymer Films

CIGS and PSS film was deposited using LbL process on ITO-coated glass and the I/V characteristics were measured using the Keithley Instrument. The results are shown in Figure 5.2.1. An ITO-coated glass with a 500 μm wide channel was alternately dipped in aqueous dispersions of CIGS nanoparticles and 3mg/ml PSS. The substrate was dipped in each solution for 5 minutes with intermediate water washing steps. After each 2 bi-layers the sample was dried and I/V characteristics were measured. The I/V results of the sample for no layer and 2, 4, and 6 bi-layers are shown in Figure 5.2.1.

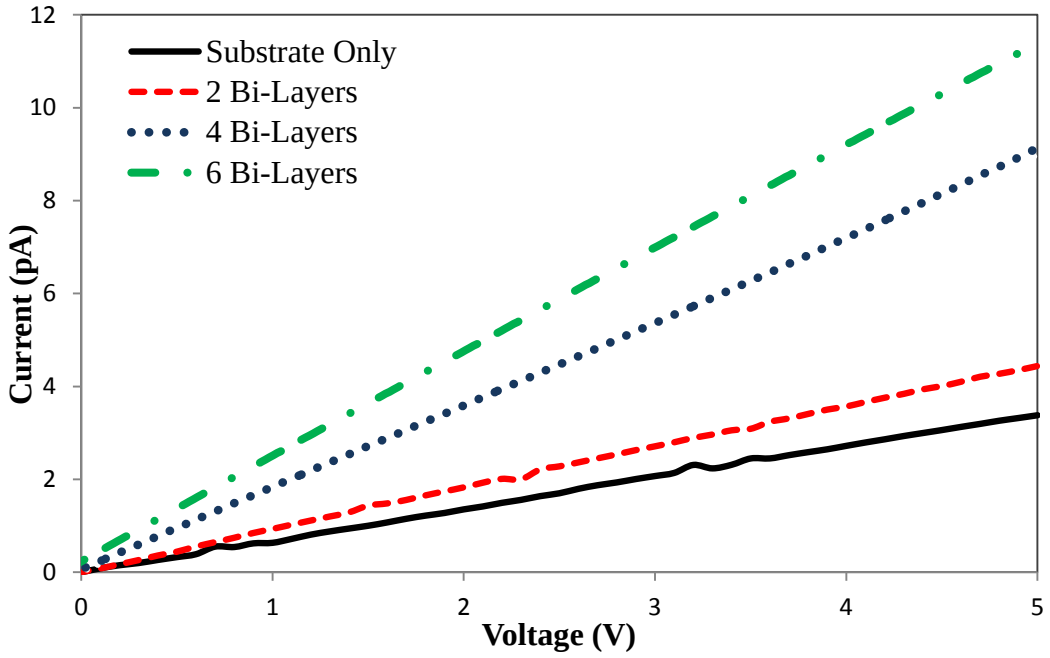

Figure 5.2.1 The I/V characteristics of CIGS/PSS LbL deposited film on an ITO coated glass

As expected, the resistance of the film decreased with the deposition of each additional layer. The small current is attributed to the relatively high resistance of the thin film in the channel stem from a wide (500 μm) channel and a thin layer of CIGS film, intermingled with insulated PSS polymer. An experiment similar to the one described above was performed for CIGS and PSS film, with an additional annealing step at 240˚C for 10 minutes after every 2 bi-layer deposition. I/V characteristics were measured after

every 2 bi-layers. The results are shown in Figure 5.2.2. A decrease in resistivity of the film by 76.4% from 0.4MΩ.m to 0.1 MΩ.m was observed.

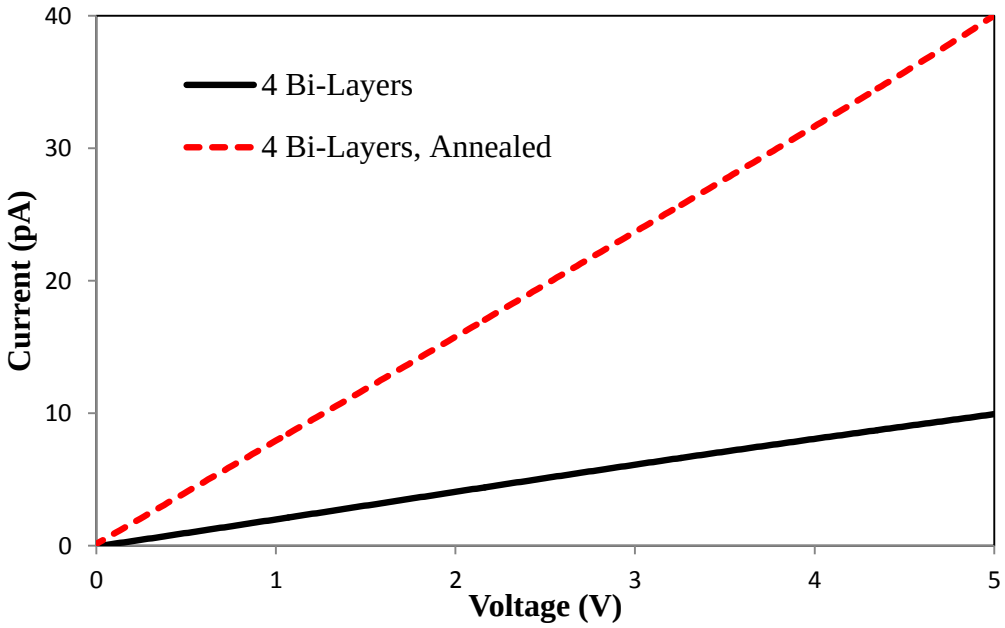

Figure 5.2.2 The I/V characteristics of a 6 bi-layer CIGS-PSS LbL films (annealed after each 2 bi-layers at 240˚C for 10 min), showing the decrease in resistivity by 76.4%

In further experiment, CIGS-PSS/PEI film using functionalized CIGS with PSS, as discussed in Section 3.4, was deposited using the LbL process on an ITO-coated glass and the I/V characteristics were measured using the Keithley Instrument. Figure 5.2.3 shows the I/V characteristics of 6 bi-layers of PSS coated CIGS and PEI. An ITO coated glass with a 500 μm wide channel was alternately dipped in aqueous dispersions of CIGS nanoparticles coated with PSS and 3mg/ml PEI, for 5 minutes each. An increase in current of the film was seen after each bi-layer addition. The resistivity of the film was decreased from 47.9 MΩ.m to 2.4 MΩ.m after a 6 bi-layer deposition. The light effect on the 6 bi-layer film is also presented which shows that under light illumination (100 W light source) the resistivity of the film decreased by 60% to 1 MΩ.m.

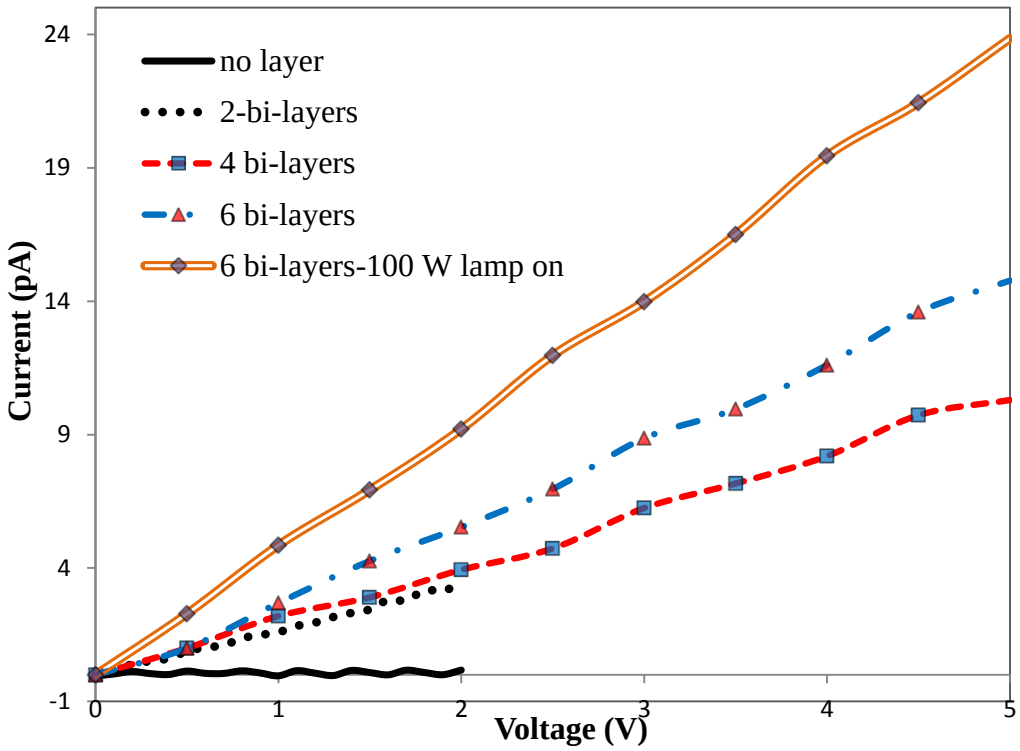

Figure 5.2.3 The I/V characteristics of 6 bi-layers of CIGS-PSS and PEI. The film resistivity decreases after deposition of each bi-layer. Also showing the decrease in resistivity by light illumination

The annealing effect on the PSS coated CIGS and PEI LbL film was conducted for 1, 2, and 3 and 4 bi-layer films. The film was annealed at 150 ˚C for 5 minutes. Comparing the resistivity, the current value of the 4 bi-layer film after annealing (Figure 5.2.4) is decreased by 87% from 0.55 MΩ.m to 0.07 MΩ.m, which means annealing lead to a more uniform film to be formed and caused the polymers and unwanted residues from the LbL solutions to be evaporated and a better interconnection between nanoparticles to be formed.

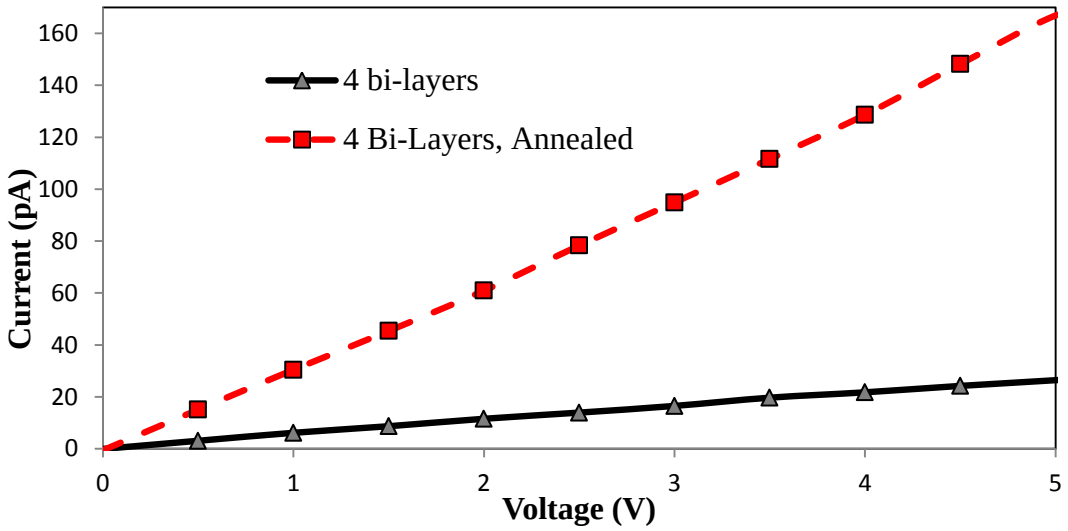

Figure 5.2.4 The I/V characteristics of a 3-bilayer CIGS-PSS and PEI LbL film before and after annealing

5.3 Summary

The layer-by-layer nanoassembly experiments were performed on a 500 μm etched channel on an ITO-coated glass substrate using negatively and positively charged CIGS (CIGS+ and CIGS–), CIGS and PSS, and CIGS-PSS and PEI. The immersion time for each of the solutions was 5 minutes. The resisitivity of the channel was measured to be 47.9 MΩ.m with no layer deposited. After the deposition of 12 LbL bi-layers of positively and negatively charged CIGS, the resistivity of the channel was decreased to 5.5 MΩ.m. For 6 bi-layers of CIGS and PSS, and 6 bi-layers of CIGS-PSS and PEI film, the channel resistance was decreased to 0.4 MΩ.m and 2.4 MΩ.m, respectively, which indicates a good film deposition.

The light effect on 12 layers of CIGS+ and CIGS–, and CIGS-PSS and PEI films were studied as well. A summary of resistivity in the dark and under light illumination for each of the CIGS film types is presented in Table 5.3.1. The best light effect was obtained for CIGS/CIGS film, which decreased the resistivity of the film by 93%, and that is because no polymer deposition was included in the LbL process and only CIGS

nanoparticles were deposited for each layer. But for both film types, decrease in resistivity after the light illumination was seen.

Table 5.3.1 Showing the resistivity of the CIGS nanoparticles LbL film in dark and under light illumination versus the number of the layers (The channel resistivity with no layer deposited is 47.9 MΩ.m)

Film Types	Number of Layers	Thickness/ Layer (nm)	Channel Width (µm)	Channel Length (cm)	Resistance (Dark) (TΩ)	Resistivity (Dark) (MΩ.m)	Resistance (Illuminated) (TΩ)	Resistivity (Illuminated) (MΩ.m)
CIGS/CIGS	12	2.25	500	2	7.4	7.9	0.5	0.5
CIGS-PSS/ PEI	12	10.2	500	2	0.5	2.4	0.2	0.97

In addition, the annealing effect on 8 layers of CIGS and PSS, and CIGS-PSS and PEI films was studied and the resistivity results are presented in Table 5.3.2. A good decrease on the film resistivity was observed. It was shown that annealing of CIGS and PSS film decreased the film resistivity by 76.4% and also annealing the CIGS-PSS/PEI film decreased the film resistivity by 87%.

Table 5.3.2 Showing the resistivity of the CIGS nanoparticles LbL film before and after annealing versus the number of the layers (The channel resistivity with no layer deposited is 47.9 MΩ.m)

Film Types	Number of Layers	Thickness/ Layer (nm)	Channel Width (µm)	Channel Length (cm)	Resistance (TΩ)	Resistivity (MΩ.m)	Resistance (Annealed) (TΩ)	Resistivity (Annealed) (MΩ.m)
CIGS/PSS	8	2.5	500	2	0.53	0.4	0.125	0.1
CIGS-PSS/ PEI	8	10.2	500	2	0.17	0.55	0.029	0.07

6 LBL CIGS FILMS FOR SOLAR CELL APPLICATIONS

6.1 Overview

Solar cell is a photodevice which generate electrical power by converting photo-energy to electrical energy. A typical solar cell consists of a p-n junction with a built-in electrical field across it. The light absorbed inside the diode creates free electron-hole pairs. If a wire is connected between the n-type to the p-type, minority carriers would flow through the wire and create electricity for an external load. Figure 6.1.1 shows a schematic image of a p-n junction solar cell [49]. The cell must be designed in a way to collect as many photogenerated minority carriers as possible and this causes less carrier recombination to be occurred in the device structure.

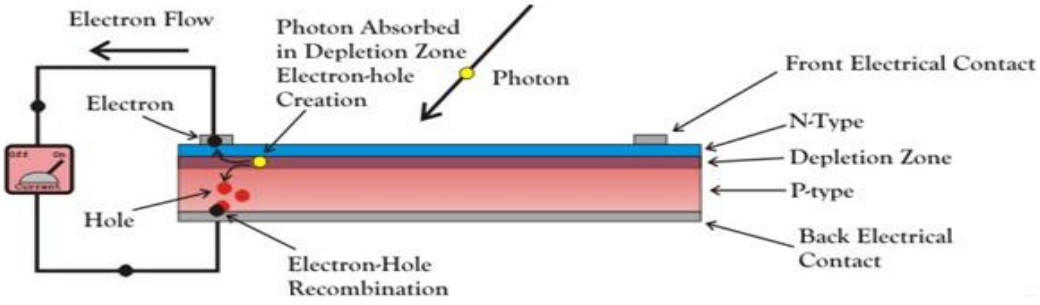

Figure 6.1.1 Schematic of a p-n junction solar cell [50]

Electron-hole pairs can be generated in the depletion region either thermally when there is no light (I_{dark}) or by absorbing the energy from photons (I_L). Thus, the current (I) in a p-n photodiode is calculated using Equation 6.1 [51].

$$I = I_{dark} + I_L \tag{6.1}$$

The dark current component (I_{dark}) for an ideal case is measured using Equation 6.2. A schematic of an ideal diode I/V curve is presented in Figure 6.1.2. In the ideal case, leakage current (I_o) is typically very small (~10^{-14}A) [51].

$$I_{dark} = I_0(e^{\frac{qV_A}{KT}} - 1) \tag{6.2}$$

Where q (c) is the magnitude of the electric charge, V_A (V) is the bias voltage, K is the Boltzmann constant, and T is the temperature (K) [51, 52].

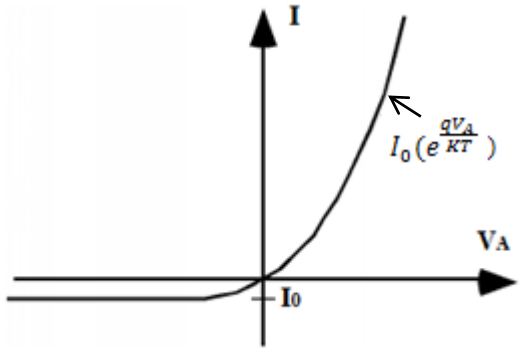

Figure 6.1.2 Ideal diode I/V characteristics

The light current component I_L is a reverse-going component of the diode current and is equal to –q times the electron-hole pairs generated per second due to the light illumination in the volume A (L_N + W + L_P), where A is the illuminated cross section area, L_N and L_P are electron and hole minority carrier diffusion length, respectively, and W is the depletion width. Thus I_L is calculated using Equation 6.3 [51].

$$I_L = -q(L_N + W + L_P)G_L \tag{6.3}$$

In Equation 6.3, G_L represents the photogeneration rate and it is assumed to be uniform throughout the diode. Since W is very small in a p-n junction compare to (L_N + L_P), and if this term (W) is considered as negligible, I_L become independent of the applied bias and the I/V characteristics of the diode is moving downwards by increasing the light intensity (increasing G_L) [51]. Figure 6.1.3 shows the I/V characteristics of a photodiode (solar cell) in dark and under illumination [53]. The solar cell parameters such as open circuit voltage (V_{oc}), shor circuit current (I_{sc}), and maximum power (P_{max}) is shown on the figure. It is clear that $P_{max} = I_m V_m$ is always smaller than $P = I_{sc} V_{oc}$.

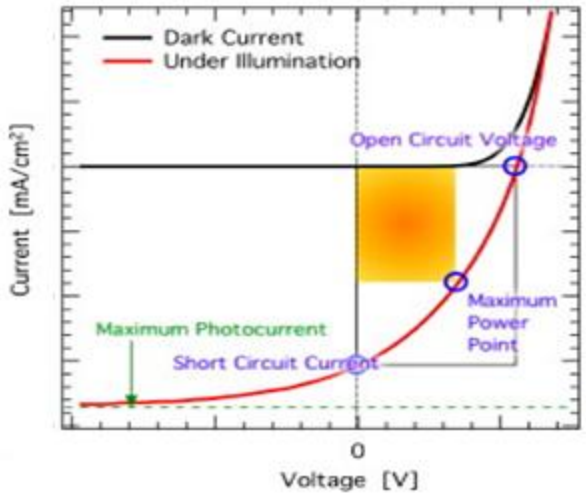

Figure 6.1.3 Schematic of solar cell I/V characteristics in the dark and under light illumination [54]

The configuration of thin film solar cells can be either superstrate or substrate structure [55]. When the superstrate structure is used, the back contact is transparent with a metal oxide back contact. This configuration can be illuminated by light from both sides, but for the substrate structure, the substrate back contact is a metal which is not transparent. Depending on deposition methods which are applied for material depositions, substrate can be either flexible or rigid. Expensive rigid substrates (ceramics, special glasses) are used when high-temperature deposition methods are involved and flexible substrates are used when the process is handling at low temperature (less expensive). In CIGS thin film solar cells both of superstrate and substrate configurations are used but higher efficiency for the substrate configuration has been reported [11].

In a CIGS solar cell, CIGS forms p-type material while n-type could be chosen from a list of n-type materials with high band gaps for a high throughput. In CIGS solar cells, CdS is usually used as the n-type material because of its wide band gap [56]. The CdS layer should be very thin to minimize the resistive losses and thus raise the efficiency. In most of the CIGS solar cells, a highly conductive layer of ZnO (n-ZnO) is used for the carrier collection just before the front contact and a very thin layer of highly-resistive ZnO (i-ZnO) as buffer layer is applied between CdS and conductive ZnO which helps to enhance the solar cell efficiency [57]. CdS layer thickness could also be reduced to less than 20 nm by using this bi-layer of ZnO [57].

6.2 Fabrication and Testing Methods

CIGS solar cells were fabricated with the CIGS and other material layers as discussed in the previous section and tested using the Keithley Semiconductor Characterization Instrument. All the materials used in the fabrication were solution based and were deposited at room temperature and in the air environment (vacuum or glove boxes were not used for any of the device fabrication processes).

The back contact of the solar cell plays an important role in determining the operation and efficiency of the solar cells, usually determined by the work function of the material [58]. As CIGS is a p-type semiconductor; the back contact should be a material with higher work function than CIGS to be able to form an ohmic junction [55]. Since the work function of CIGS is higher than most of the metals, they are not suitable to be used as the back contact for the CIGS solar cell. However, some metals, such as molybdenum (Mo) under high temperature can form chemical bonding with the selenium element in the CIGS structure forming an ohmic contact, thus can be used as a back contact. Some other materials such as conductive oxide (such as indium tin oxide, ITO) and conductive polymers poly (3, 4-ethylenedioxythiophene) (PEODT) have also been known to form a good ohmic contact with the CIGS. Mo, ITO, and PEDOT were considered for the fabrication of the solar cells.

Layer by layer, chemical bath deposition (CBD), drop casting, and spin coating methods were used for the deposition of the various layers of the solar cell. To achieve a very thin and transparent layer for the front contact fabrication, solutions of n-type ZnO, Intrinsic ZnO and CdS in different dispersants were deposited on the ITO-coated glass through the spin-coating method. In the spin-coating method, a uniform and stable solution of the particles is needed; otherwise particles would not be deposited uniformly. Thus, the dispersant for various materials may be differed. When the solution is prepared, the substrate, which is held by the vacuum on the spinner, should be covered by enough amounts of the solution, then depending on the dispersant, the spinning time and speed will be determined. For the following experiments, the spinning of IPA-based solutions was started at 500 rpm and increased to 1000 rpm in few seconds, and left at that speed until the substrate dried (about 1 minute). For the water-based solutions, the spinner speed was set to 500 rpm and remained spinning until the substrate dried (about 5 minutes). The drop-casting method was also used to deposit CIGS nanoparticles and also CdS for one of the devices.

In order to test the devices, four micromanipulator probes of the Keithley measurement instrument were used. Two probes were used on each side of the sample, as shown in Figure 6.2.1. This method can minimize the effect of contact resistance between the probe and the substrate and also the effect of the probe resistance itself.

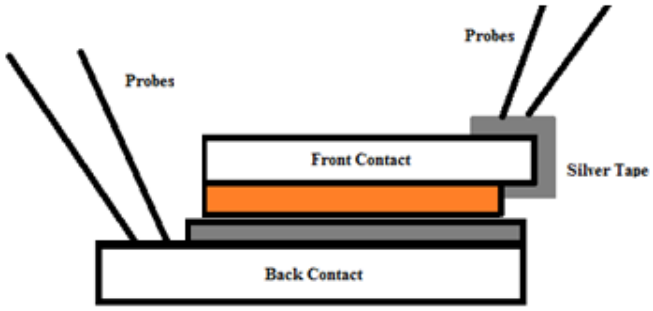

Figure 6.2.1 Schematic of the probes placements on the device to measure the I/V characteristics

Since CIGS and PEDOT have ohmic contact, PEDOT was used as back contact material. PEDOT was drop-casted on the glass substrate and heated at 250˚C for 15 minutes. CIGS nanoparticles dispersed in IPA were drop-casted on the PEDOT film at room temperature. A layer of n-type/intrinsic ZnO was spin-coated on an ITO-coated glass. The two substrate plates then were assembled together as shown in Figure 6.2.2.

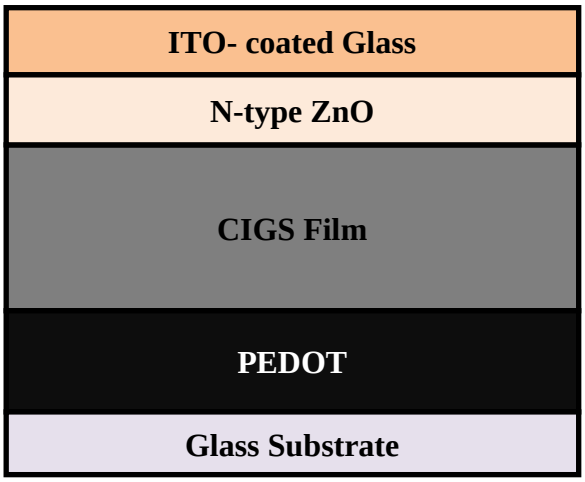

Figure 6.2.2 Schematic of PEDOT-CIGS -n-ZnO solar cell device (Device-I) with ITO as front contact.

The band diagram of the device is shown in Figure 6.2.3. In this structure PEDOT is heavily doped p-type organic semiconductor and ZnO is heavily doped n-type material, their band gaps are much higher than the CIGS, CIGS is working as an absorber and the device forms a p-i-n solar cell [23].

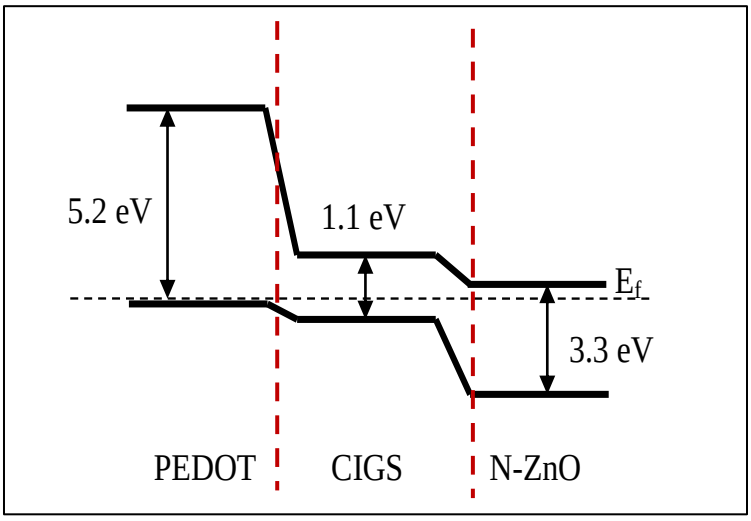

Figure 6.2.3 Energy band diagram of PEDOT-CIGS-n-ZnO device (Device-I) at equilibrium

A p-i-n diode is a junction between a heavily doped p- and n-type with an intrinsic (lightly doped) material sandwiched in between. Because the depletion region between heavily doped p- and n-type martials is very narrow, therefore the depletion width inside the device is about the same as the intrinsic region (i-layer) width. Thus the most part of the generated current in a p-i-n device are formed by carrier generation in the depletion region (i-layer) under light illumination. Since i-layer is lightly doped, it is totally depleted under zero bias or becomes depleted under a very small reverse bias.

In the next phase of devices, CdS was used as n-type material and to form a junction with CIGS, and ITO was used both as front and back contact. The CdS and CIGS films were fabricated by the drop-casting deposition method. An ITO-coated substrate was covered using a concentrate (3 mg/ml) aqua solution of CdS and heated at 90˚C for 90 minutes, and then the temperature was raised to 450 ˚C for 30 minutes. On the other hand, concentrated solution of CIGS was drop-casted on another ITO-coated substrate at room temperature. The device was then assembled as shown in Figure 6.2.4.

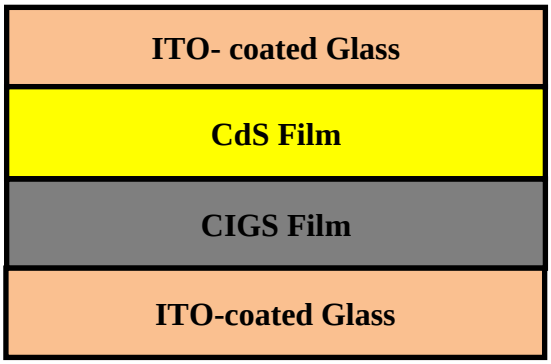

Figure 6.2.4 Schematic of CIGS-CdS solar cell device (Device-II) with ITO as front and back contacts

In another device, molybdenum (Mo) was used as the back contact, and CdS was used as the n-type material. CdS is an n-type semiconductor with a direct band gap and unique photoconductive, electrical, and optical properties. The band gap of CdS at room temperature is 2.42 eV [59]. Due to the mentioned unique properties, CdS is a suitable n-type semiconductor for thin film solar cells. In addition to forming a p-n junction, a layer of intrinsic zinc oxide (i-Zno) and a layer of n-type zinc oxide (n-ZnO) were used to improve the current of the device. The addition of n-ZnO layer before the ITO helps to minimize any junction between ITO and CdS. The addition of the i-ZnO layer prevents shorting of CdS layer while depositing n-Zno.

For the device fabrication, first, 0.3 g of n-ZnO nanopowder, having low electrical resisance, was dispersed uniformly in 4 ml of isopropyl alcohol (IPA) and two thin layers of this solution was spin-coated on an ITO coated substrate. In almost all of the thin film solar cells, because ITO is a heavily doped n-type semiconductor, it is considered as the metallic contact [24]. After the deposition, substrate was heated for 2 minutes at 105 ˚C. Then 2 layers of intrinsic ZnO (i-ZnO) with high resistance were spin-coated on top of the previous layer using the same concentration. The substrate was heated then for 2 minutes at 105 ˚C. These layers on ITO form the transparent front contact part of the solar cell where the light is illuminated. Then water-dispersed CdS was drop-casted on top of the other layers when the substrate was at 105 ˚C on the hot plate. After the water

of the CdS solution dried, the whole substrate was baked at 540 ˚C for 30 minutes. The schematic of the above mentioned device is shown in Figure 6.2.5. The band diagram of the Device-III is shown in Figure 6.2.6.

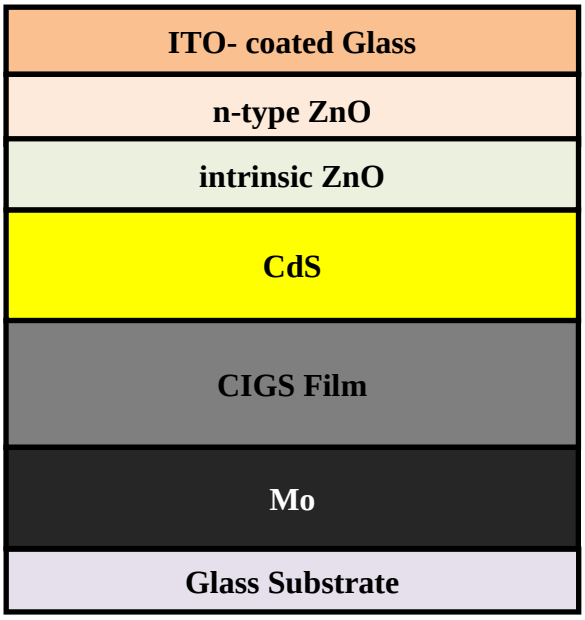

Figure 6.2.5 Schematic shows of CIGS-CdS, solar cell device (Device-III) with ZnO buffer layers and Mo as back contact and ITO as front contact

As shown in Figure 6.2.6, CdS (n-type) and CIGS (p-type) form a p-n junction since both have almost the same doping. In this device ZnO is heavily doped n-type semiconductor and is used as the buffer layer before the front contact.

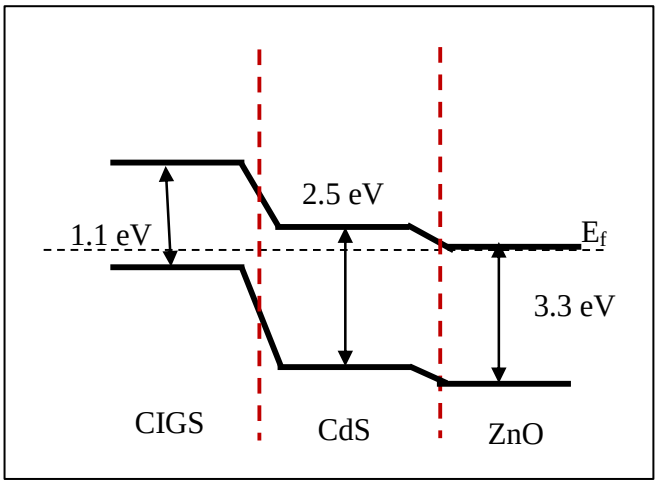

Figure 6.2.6 Energy band diagram of CIGS-CdS device (Device-III) at equilibrium

In another experiment (Device-IV), LbL deposited CIGS on the ITO substrate was used as the active CIGS layer. As CIGS-PSS and PEI deposited LbL film showed good film build up and also good conductivity, it has been used for solar cell fabrication. PSS-coated CIGS was prepared as described in Section 4.4, 6.25 mg/ml concentration of CIGS-PSS solution and 3 mg/ml of PEI were used. An ITO substrate was cleaned using acetone, IPA, and DI-water, and 13 bi-layers of CIGS-PSS and PEI were deposited sequentially. The substrate was dipped for 15 minutes in CIGS-PSS solution, washed in water for 5 minutes (3-step washing), dipped in PEI solution for 5 minutes, and washed in water again through the mentioned 3-step washing procedure. CdS was then deposited on the CIGS film using chemical bath deposition (CBD) [56]. A sequential spin coating of n-ZnO doped with Aluminum (ZnO:Al) and i-ZnO, was performed on the fabricated LbL film to form the solar cell. The device structure is similar to Device-III.

6.3 Results and Discussion

I/V characteristics of the solar cell devices discussed in the previous section were measured using the Keithley 4200-SCS semiconductor measurement instrument. The experiments were conducted in the dark (when all the light sources of the laboratory were

turned off), ambient room light, and under additional light illuminated towards the devices. It was observed that the difference between I/V characteristics results of the devices measured in the dark and under ambient light were negligible. Thus, for the I/V measurement results showing light effect, the ambient light was taken as the dark condition and additional light were shined on the devices for light illuminated results. The results presented in this section were obtained from the devices having the active area of 1 cm^2. Figure 6.3.1 shows a solar cell device under measurement using Keithley instrument and a microscope.

The I/V characteristics of Device-I (the device structure is shown in Figure 6.2.2) is presented in Figure 6.3.2. The device was tested in the dark and under illumination by 200 W light source. It was observed that the device shows solar cell characteristics, however short circuit current (J_{sc} = 0.02 $\mu A/cm^2$) measured at zero voltage was small. It was also observed that at zero voltage, J_{sc} increased with increase in the light intensity (J_{sc} = 0.06 $\mu A/cm^2$). The open circuit voltage for this device was measured to be (V_{oc}) 0.3 V yielding the maximum power density of 0.018 nW/cm^2.

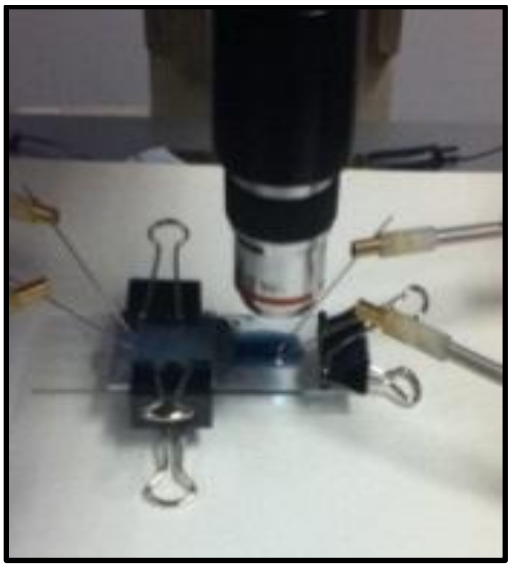

Figure 6.3.1 Showing Device-I under measurement

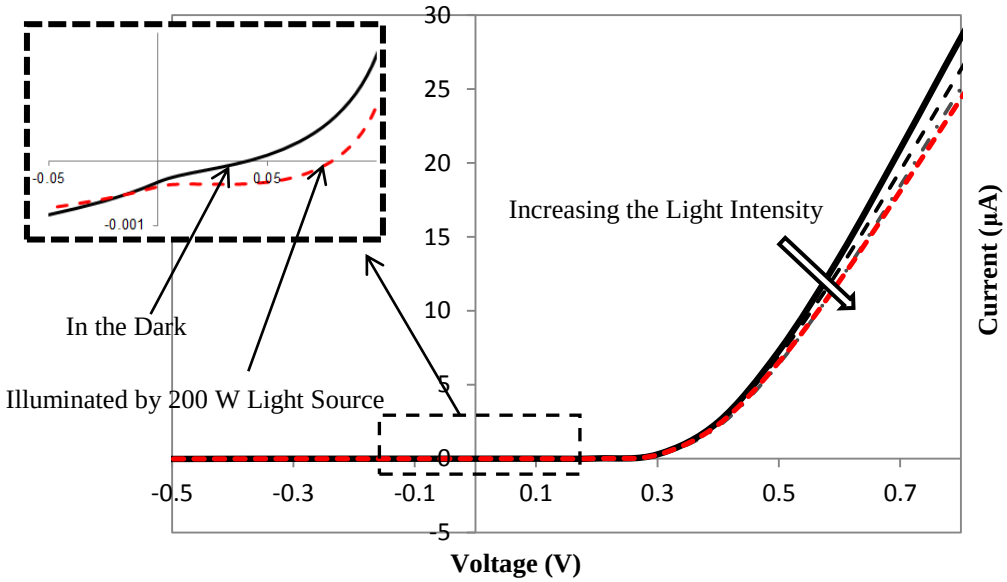

Figure 6.3.2 The I/V characteristics of a PEDOT-CIGS-ZnO solar cell using ITO as front contact (Device-I)

The measured I/V characteristics of Device-II are shown in Figure 6.3.3. The device was illuminated by 300 W light source. It was observed that the curve moved down under light illumination and showed a diode characteristic as well. The short circuit current density and open circuit voltage were measured to be 0.05 nA/cm^2 and 0.2 V, respectively, yielding the power density of 0.01 nW/cm^2.

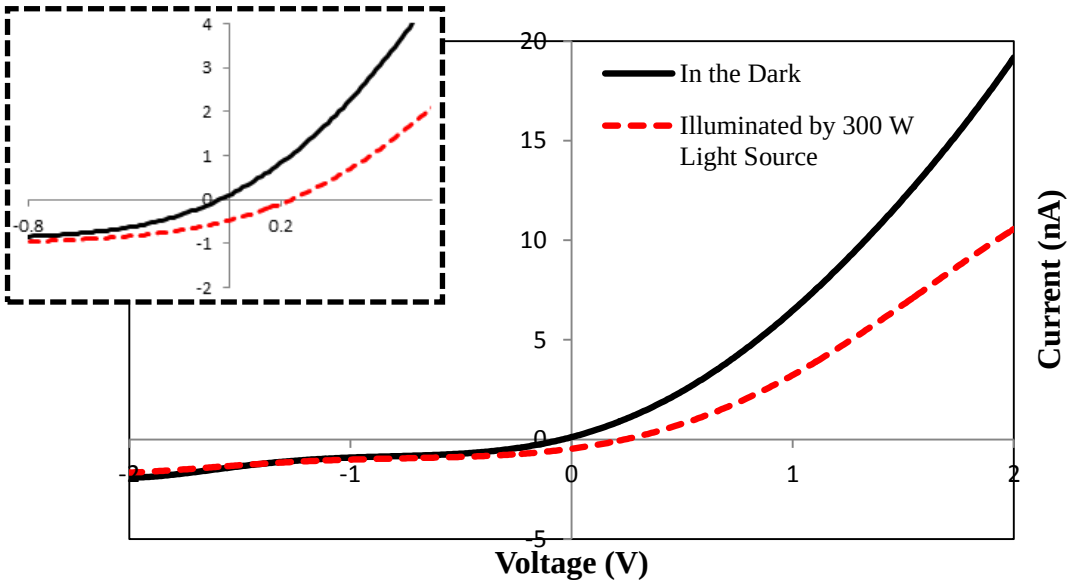

Figure 6.3.3 The I/V characteristics of a CdS, and CIGS solar cell configuration using ITO as both back and front contact (Device-II)

Figure 6.3.4 shows the I/V characteristics of Device-III in dark and under 100 W light source illumination. As depicted in the image (closer view to the zero voltage), the solar cell reacts to light and the open circuit voltage is 10 mV and the short circuit current density is measured to be 50 nA/cm^2, yielding a power density of 0.5 nW/cm^2. By making the light on and off on the device, the light effect was observed (red line). In this case since the light was illuminated from top of the device and CIGS was covered with a thick layer of CdS, very small amount of light could reach the CIGS top surface to generate electron-hole pairs. Therefore the photogenerated current is very small.

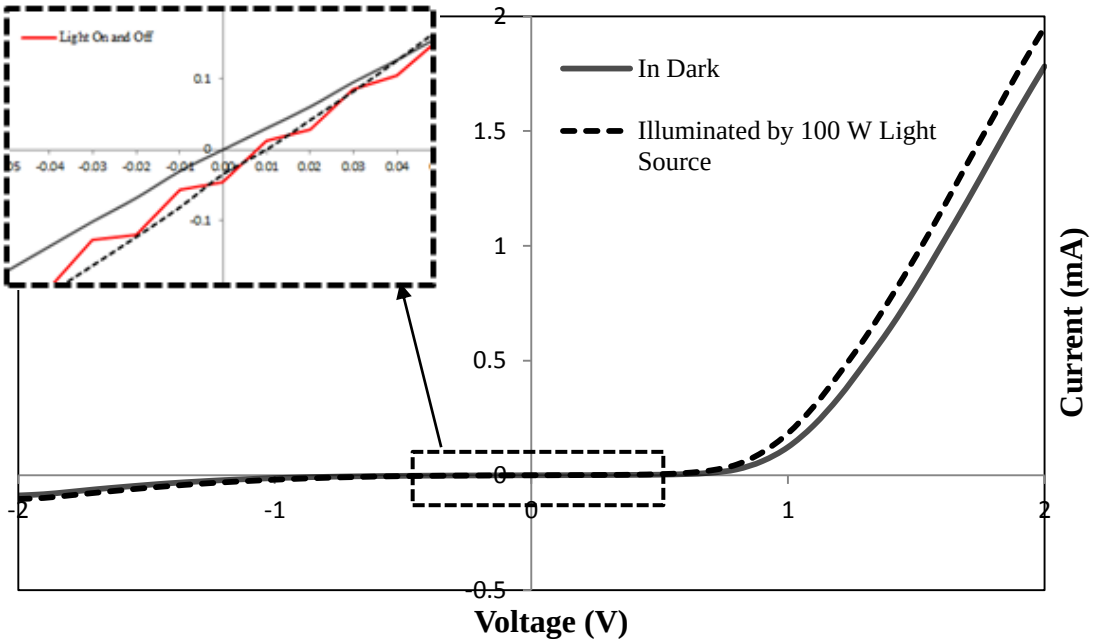

Figure 6.3.4 Solar cell results of CIGS and CdS configuration using n-ZnO and i-ZnO as buffer layers, and Mo as back contact and ITO as front contact (Device-III)

The I/V characteristics results for Device-IV using 13 bi-layers of CIGS-PSS and PEI film is presented in Figure 6.3.5. This result has been obtained under 50 W light source illumination. As presented, the device showed a better solar cell characteristic than Device-III and its current is comparable to Device-III, although the film thickness is much less than that of Device-III (much less material was used), However the fabrication process needs to be further improved in order to have a better device I/V characteristics. The short circuit current density (J_{sc}) at 0 V and open circuit voltage (V_{oc}) for Device-IV are measured to be about 25 μA/cm^2 and the and 0.045 V, respectively and the power density is measured to be 1.125 μW/cm^2. This results show a 99% increase in the power density and efficiency by using the LbL CIGS nanoparticles film.

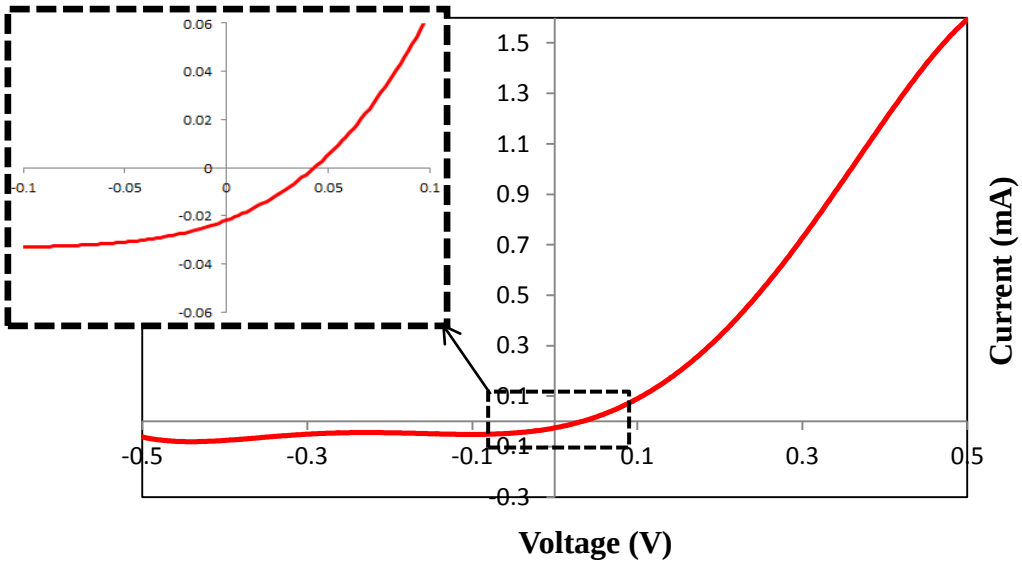

Figure 6.3.5 Solar cell results of LbL CIGS film and chemical bath deposited CdS configuration using n-ZnO and i-ZnO as buffer layers, and ITO as both back and front contact (Device-IV)

In a different experiment, a 13 bi-layer CIGS film was deposited on an ITO-coated substrate and sandwiched between the substrate and another ITO-coated glass which was coated with n-ZnO and i-ZnO through spin-coating (Device-V). The I/V characteristics of Device-V is presented in Figure 6.3.6. The device was illuminated by a 50 W light source and the photovoltaic effect is clearly shown. An increase in current was seen by raising the light intensity, but, since n-ZnO is heavily doped n-type, thus the junction was not perfectly p-n junction and is more similar to an ohmic junction.

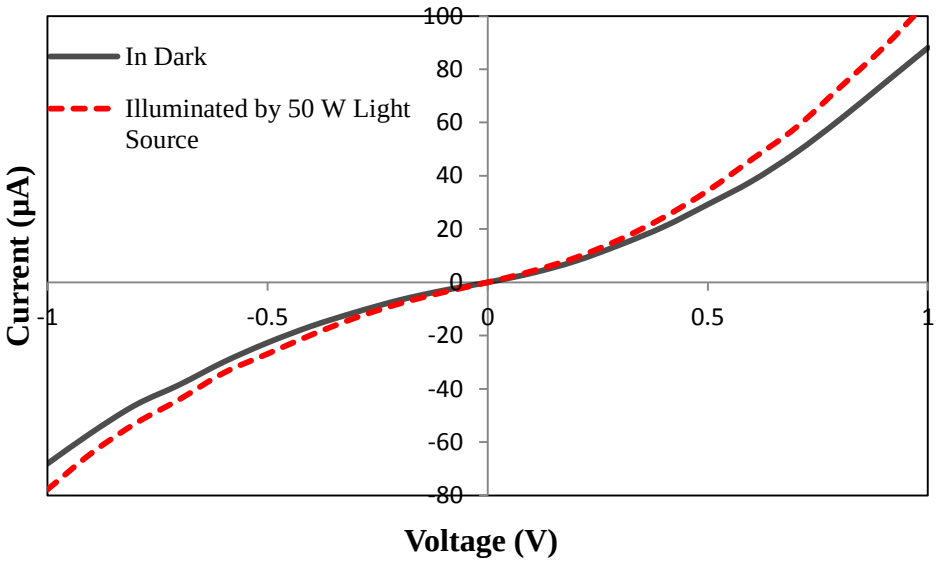

Figure 6.3.6 Solar cell results of LbL CIGS film, n-ZnO, i-ZnO configuration using ITO as both back and front contact (Device-V)

In Table 6.3.1, comparisons of the power densities among the fabricated solar cell devices are presented. As shown the best power density with a huge difference was obtained by using the LbL CIGS film.

Table 6.3.1 Comparison of the power density for the fabricated solar cell devices

Device	Power Density
Device-I (Drop-casted CIGS Film)	0.018 nW/cm^2
Device-II (Drop-casted CIGS Film)	0.01 nW/cm^2
Device-III (Drop-casted CIGS Film)	0.5 nW/cm^2
Device-IV (LbL CIGS Film)	1.125 µW/cm^2

7 CONCLUSION AND FUTURE WORK

7.1 Conclusion

In this research study, $Cu(InGa)Se_2$ (CIGS) nanoparticles were synthesized, functionalized using PSS to disperse in water, and further utilized in LbL film fabrication. After coating the CIGS nanoparticles with PSS, the size of the particle decreased. Particles were able to disperse in water uniformly coating with PSS. Then the Layer-by-Layer (LbL) nanoassembly method was utilized with oppositely charged aqua solutions of (CIGS) nanoparticles. Positive and negative charged CIGS nanoparticles were obtained by surface functionalization of the particles with polystyrene sulfonate (PSS) coating and also by raising the pH of the solution. The zeta potential of the particles in water was measured to be +61 mV and after coating with PSS and raising the pH of the solution was reversed to −56.9 mV and −43.4 mV, respectively.

LbL depositions were conducted using CIGS and PSS and CIGS-PSS and PEI on a quartz crystal microbalance (QCM) and resulted in each layer thickness of 1.3 nm and 10.2 nm, respectively. Subsequently, CIGS films were deposited on glass and ITO coated glass substrate and the electrical properties of the film were measured using the Keithley semiconductor characterization system. It was observed that the conductivity of the film increases after each layer deposition. It was also shown that the conductivity was increased by light illumination as well as by annealing the film. QCM and I/V characteristic results of the fabricated films were also presented and discussed.

This work mainly focused on synthesis of CIGS nanoparticles, fabricating LbL film using the CIGS nanoparticles, and characterizing the fabricated films using I/V

measurement. In addition, preliminary studies with fabrication and testing of CIGS solar cells were also conducted. The preliminary results have been encouraging; however, there is still a good room for improvement which is discussed in Future Work, Section 7.2. The functionalized nanoparticles and the LbL CIGS films were used in the solar cell devices. Several configurations of CIGS films (p-type), and ZnO and CdS films (n-type) were considered and devices were characterized by the Keithley semiconductor characterization instrument and micromanipulator probing station. The results showed that using LbL CIGS nanoparticles film improve the solar cell efficiency and power generation.

Moreover, CdS and ZnO nanoparticles were functionalized using PSS to disperse in water uniformly and the LbL nanoassembly was performed to deposit PSS-coated CdS and ZnO on ITO glass using PEI. The film thickness of 30 nm and 140 nm were obtained respectively, while the smallest particle size of CdS was measured to be 9 nm and was measured to be 40 nm for ZnO.

7.1 Future Work

Most of the work conducted under this thesis research focused on developing and characterizing LbL films of CIGS. While some results on solar cells are presented a good of work would be needed to develop a high efficiency all-LbL solar cell. The future work on this research will be on developing the solar cell using all-LbL layers, improving the process, and efficiency, and obtaining the solar cells on flexible substrates. Some key future works are highlighted bellow:

- CIGS nanoparticles can obtain better electrical conductivity and optical properties through ligand exchange treatment with new materials like 1,2-Ethanedithiol (EDT) or Methiopropamine (MPA). The experiments are currently running and are still under study [47].

- Since LbL CIGS film could improve the solar cell efficiency, The LbL film of CdS and ZnO (n-type and intrinsic) can be implemented in the solar cell device structure as well.

- Back contact of the solar cell should be improved to avoid the small schottky junction formation and thus increase the current.

Since the LbL nanoassembly process is readily scalable and can be conducted on any substrate (solid and flexible), paper-based CIGS solar cells can be fabricated using CIGS nanoparticles LbL film on a flexible conductive substrate and applying paper-based carbon nanotube (CNT) sheets as the back contact. Very high efficiency and low costs can be obtained using this structure. Paper-based CIGS solar cells can be a very good power supply for micro fluidic devices or any of low power consumers.

LIST OF REFERENCES

LIST OF REFERENCES

[1] F. de Winter and R. B. Swenson, "A Wake-up Call," Solar Today, 2006.

[2] "Photovoltaics- Technical Background," European Commissions Reasearch and Innovation, [Online]. Available: http://ec.europa.eu/research/energy/eu/research/photovoltaics/index_en.htm. [Accessed October 2011].

[3] German Advisory Council on Global Change, 2003. [Online]. Available: www.wbgu.de. [Accessed January 2011].

[4] S. Schleußner, "Cu(In,Ga)Se2 Thin Film Solar Cells with ZrN as a Back Contact," IPE, Stuttgat, Sweden, 2003.

[5] H. Lund, R. Nilsen, O. Salomatova, D. Skare, and E. Riisem, "The History Highlight of Solar Sells (Photovoltaic Cells)," 2008. [Online]. Available: org.ntnu.no/solarcells. [Accessed November 2011].

[6] "Timeline of solar cells," Wikimedia Foundation, Inc., 2004. [Online]. Available: http://www.enotes.com/topic/Timeline_of_solar_cells. [Accessed December 2011].

[7] H. Sinchu, "Global PV Market Trend & Development," 2008. [Online]. Available: http://www.semiconrussia.org/SCTAIWAN-CT/ProgramsandEvents/STS/cms/groups/public/documents/web_content/ctr_012376.pdf. [Accessed May 2011].

[8] L. Kazmerski, "NREL Compilation of Best Research Solar Cell Efficiencies," National Renewable Energy Laboratory (NREL), 2011.

[9] S. Byrnes, "Shockley-Queisser Full Curve," Wikipedia, 2011.

[10] B. von Roedern and H.S. Ullal, "Thin Film CIGS and CdTe Photovoltaic Technologies: Commercialization, Critical Issues, and Applications," in *22nd European Photovoltaic Solar Energy Conference (PVSEC) and Exhibition*, Milan, Italy, 2007.

[11] K. L. Chopra, P. D. Paulson, and V. Dutta, "Thin-Film Solar Cells: An Overview," *Progress in Photovoltaics: Research and Applications,* vol. 12, no. 2-3, pp. 69-92, March/May 2004.

[12] I. Repins, M. A. Contreras, B. Eggas, C. DeHart, J. Scharf, C. L. Perkins, B. To, and R. Noufi, "19.9%-efficient ZnO/CdS/CuInGaSe2 Solar Cell with 81.2% Fill Factor," *Wiley Inter Science,* vol. 16, no. 3, pp. 235-239, February 2008.

[13] K. Ramanathan, M. A. Contreras, C. L. Perkins, S. A., F. S. Hasoon,J. Keane, D. Young, M. Romero, W. Metzger, R. Noufi, J. Ward, and A. Duda, "Properties of 19.2% Efficiency ZnO/CdS/CuInGaSe2 Thin-film Solar Cells," *Progress in Photovoltaics: Research and Applications,* vol. 11, no. 4, p. 225–230, 2003.

[14] S. Bowden, U. Das , S. Herasimenka, and R. Birkmire, "Stability of Amorphous/Crystalline Silicon Heterojunctions," in *Photovoltaic Specialists Conference*, Newark, Delaware, 2008.

[15] V. Kapur, A. Bansal, P. Le, and O. I. Asensio, "Non-vacuum Processing of CuIn1-xGaxSe2 Solar Cell on Rigid and Flexible Substrates using Nanoparticle Precursor Inks," *Thin Solid Films 431-432*, pp. 53-57, 2003.

[16] M. A. Contreras, B. Egaas, K. Ramanathan, J. Hiltner, A. Swartzlander, F. Hasoon and R. Noufi, "Progress Toward 20% Effciency in Cu(In,Ga)Se2 Polycrystalline Thin-Film Solar Cells," vol. 7, no. 4, pp. 311-316, 1999.

[17] M. Powalla, G. Voorwinden, D. Hariskos, P. Jackson, and R. Kniese, "Highly Efficient CIS Solar Cells and Modules Made by the Co-evaporation Process," *Thin Solid Films,* vol. 517, no. 7, pp. 2111-2114, February 2009.

[18] T. Nakada, Y. Hirabayashi, T. Tokado, and D. Ohmori, "Cu(In1-x,Gax)Se2 Thin Film Solar Cells Using Transparent Conducting Oxide Back Contacts for Bifacial and Tandem Solar Cells," *Japanese Journal Of Applied Physics Part 2 Letters,* vol. 41, no. 11A, pp. L1209-L1211, 2002.

[19] M. Kaelin, D. Rudmann, and A. N. Tiwari, "Low Cost Processing of CIGS Thin Film Solar Cells," *Solar Energy,* vol. 77, p. 749–756, 2004.

[20] S. J. Ahn, K. H. Kim, and K. H. Yoon, "Nanoparticle Derived Cu(In, Ga)Se2 Absorber Layer for Thin Film Solar Cells," *Colloids and Surfaces A: Physicochemical Engineering Aspects,* Vols. 313-314, p. 171–174, 2008.

[21] W. Liu, D. B. Mitzi, S. J. Chey, and A. Kellock, "CuIn(Se,S)2 Absorbers Processed using a Hydrazine-Based Solution Approach," vol. 1123, 2009.

[22] A. de Kergommeaux, A. Fiore, N. Bruyant, F. Chandezon, P. Reiss, A. Pron, R. de Bettignies, and J. F. Vincent, "Synthesis of Colloidal CuInSe2 Nanocrystals Films for Photovotaic Applications," *Solar Energy Materials & Solar Cells,* vol. 95, no. 39-43, February 2011.

[23] J. A. Spies, R. Schafer, J. F. Wager, P. Hersh, H. A. S. Platt, D. A. Keszler, G. Schneider, R. Kykyneshi, J. Tate, X. Liu, A. D. Compaan, and W. N. Shafarman, "Pin Double-heterojunction Thin-film Solar Cell p-layer Assessment," *Solar Energy Materials & Solar Cells,* vol. 93, no. 8, p. 1296–1308, August 2009.

[24] J. F. Wager, "Transparent Electronics: Schottky Barrier and Heterojunction Considerations," *Thin Solids Films,* vol. 516, no. 8, February 2008.

[25] J. Kalowekamo and E. Baker, "Estimating the Manufacturing Cost of Purely Organic Solar Cells," *Solar Energy,* vol. 83, no. 8, pp. 1224-1231, 2009.

[26] J. M. Luther, M. Law, M. C. Beard, Q. Song, M. O. Reese, R. J. Ellingson, and A. J. Nozik, "Schottky Solar Cells Based on Colloidal Nanocrystal Films," *Nano Letters,* vol. 8, no. 10, 2008.

[27] J. Tang, X. Wang, L. Brzozowski, D. A. R. Barkhouse, R. Debnath, L. Levina, and E. H. Sargent, "Schottky Quantum Dot Solar Cells Stable in Air under Solar Illumination," *Advanced Materials,* vol. 22, no. 12, p. 1398–1402, 2010.

[28] "Pn-junction-equilibrium-graphs," 2010. [Online]. Available: en.wikipedia.org. [Accessed November 2011].

[29] M. A. Green, K. Emery, Y. Hishikawa, and W. Warta, "Solar Cell Efficiency Tables," *Progress in Photovoltaics: Research and Applications,* vol. 18, p. 346–352, 2010.

[30] M. Pagliaro, R. Ciriminna, and G. Palmisano, Flexible Solar Cells, vol. 1, Wiley Inter Science, 2008, pp. 880-891.

[31] M. D. Gerngroß and J. Reverey, "CIS/CIGS Based Thin-Film Solar Cells," [Online]. Available: http://www.tf.uni-kiel.de/matwis/amat/matwissem_en/kap_6/illustr/gerngross_reverey_paper_ws_08_1.pdf. [Accessed December 2011].

[32] M. Gloeckler and J. R. Sites, "Band-Gap Grading in Cu(In,Ga)Se2 Solar Cells," *Journal of Physics and Chemistry of Solids,* vol. 66, no. 11, pp. 1891-1894, 2005.

[33] V. Gremenok, V. Zalesski, A. Khodin, O. Ermakov, R. Chyhir, V. Emelyanov, and V. Syakersky, "Analysis of CIGS-Based Thin Film Solar Cells with Graded Band Gap," *Physica Status Solidic,* vol. 6, no. 5, p. 1237–1240, 2009.

[34] Release, Zentrum fuer Sonnenenergie-und Wasserstoff-Forshung Baden-Wuerttemberg (ZSW) Press, "Stuttgart Solar Researchers Bring a World Record to Germany ZSW Produces a Thin-film Solar Cell with 20.1 Percent Efficiency," April 2010.

[35] C. D. R. Ludwig, T. Gruhn, and C. Felser, "Indium-Gallium Segregation in CuInxGa(1-x)Se2: An Ab Initio–Based Monte Carlo Study," vol. 105, no. 2, 2010.

[36] S. Siebentritt, M. Igalson, C. Persson, and S. Lany, "The electronic structure of chalcopyrites—bands, point defects and grain boundaries," *Progress in Photovoltaics: Research and Applications,* vol. 18, no. 6, p. 390–410, 2010.

[37] O. Lundberg, M. Bodegard, J. Malmstroem and L. Stolt, "Influence of the Cu(In,Ga)Se2 Thickness and Ga Grading on Solar Cell Performance," *Progress in Photovoltaics: Research and Applications,* vol. 11, pp. 77-88, 2002.

[38] M. J. Hetzer, Y. M. Strzhemechny, M. Gao, M. A. Contreras, A. Zunger, and L. J. Brillson, "Direct Observation of Copper Depletion and Potential Changes at Copper Indium Gallium Diselenide Grain Boundaries," *Applied Physics Letters,* vol. 86, no. 16, p. 162105 (3 pages), 2005.

[39] J. Tang, S. Hinds, S. O. Kelley, and E. H. Sargent, "Synthesis of Colloidal CuGaSe2, CuInSe2, and Cu(InGa)Se2 Nanopartoicels," *Chemistry of Materials,* vol. 20, no. 22, pp. 6906-6910, September 2008.

[40] M. G. Panthani, V. Akhavan, B. Goodfellow, J. P. Schmidtke, L. Dunn, A. Dodabalapur, P. F. Barbara, and B. A. Korgel, "Synthesis of CuInS2, CuInSe2, and Cu(InxGa1-x)Se2 (CIGS) Nanocrystal “Inks” for Printable Photovoltaics," *JACS,* vol. 130, no. 49, pp. 16770-16777, July 2008.

[41] A. R. Jeong, R. H. Shin, W. Jo, M. Song, and S. Yoon, "Synthesis and Physical Properties of Cu(In,Ga)Se2 Nanoparticles and CuGaSe2 Thin-Films for Tandem cell Photovoltaic Applications," vol. 10, pp. 003432-003434, 2010.

[42] S. C. Riha, B. A. Parkinson, and A. L. Prieto, "Solution-Based Synthesis and Characterization of Cu2ZnSnS4 Nanocrystals," vol. 131, no. 34, p. 12054–12055, 2009.

[43] G. Decher, "Fuzzy Nanoassemblies: Toward Layered Polymeric Multicomposites," *Science,* vol. 277, no. 5330, pp. 1232-1237, 1997.

[44] M. Agarwal, S. Shrestha, P. Ghane, and K. Varahramyan, "Layer-by-Layer Nanoassembly of CIS Nanoparticles," in *ASME 2010 International Manufacturing Science and Engineering Conference*, Pennsylvania, 2010.

[45] K. Varahramyan and Y. Lvov, "Nanomanufacturing by Layer-by-Layer Assembly - from Nanoscale Coating to Device Applications," vol. 220, no. 1, pp. 29-37, March 2006.

[46] M. Iijima and H. Kamiya, "Surface Modification for Improving the Stability of Nanoparticles in Liquid Media," *KONA Powder and Particle Journal*, no. 27, pp. 119-129, 2009.

[47] J. M. Luther, M. Law, Q. Song, C. L. Perkins, M. C. Beard, and A. J. Nozik, "Structural, Optical, and Electrical Properties of Self-Assembled Films of PbSe Nanocrystals Treated with 1,2-Ethanedithiol," *American Chemical Society Nano,* vol. 2, no. 2, p. 271–280, 2008.

[48] M. Malmsten, *Biopolymers at Interfaces*, 2nd ed., New York: Marcel Dekker, 2003.

[49] G. G. Malliaras, J. R. Salem, P. J. Brock, and J. C. Scott, "Photovoltaic Measurement of the Built-In Potential in Organic Light Emitting Diodes and Photodiodes," vol. 84, no. 3, pp. 1583-1587, August 1998.

[50] "IMAGES E-Newsletter- Photovoltaic Cells- Generating Electricity," Scientific Instruments, [Online]. Available: www.imagesco.com. [Accessed October 2011].

[51] R. F. Pierret, *Semiconductor Device Fundamentals*, Addison-Wesley publishing company, Inc., 1996.

[52] P. Bhattacharya, *Semicondoctor Optoelectronic Devices*, 2nd ed., New Jersey: Prentice- Hall, Inc. Upper Saddle River, 1997.

[53] T. Eisenbarth, T. Unold, R. Caballero, C. A. Kaufmann, and H. W. Schock, "Interpretation of Admittance, Capacitance-Voltage, and Current-Voltage Signatures in Cu(In,Ga)Se2 Thin Film Solar Cells," *Journal of Applied Physics*, vol. 107, no. 3, pp. 034509-034509-12, 2010.

[54] C. Deibel, "Intermediate: Current-Voltage Characteristics of Organic Solar Cells," [Online]. Available: http://blog.disorderedmatter.eu/2008/03/05/intermediate-current-voltage-characeristics-of-organic-solar-cells/. [Accessed December 2011].

[55] F. J. Haug, D. Rudmann, A. Romeo, and H. Zogg, and A. N. Tiwari, "Electrical Properties of the Heterojunction In Cu(In,Ga)Se2 Superstrate Solar Cells," Vols. 403-404, pp. 293-296, February 2002.

[56] C. Gopinathan, T. Sarveswaran, and K. Mahalakshmi, "Studies on CdS Nanocrystalline Thin Films with Different S/Cd Ratios Prepared using Chemical Bath Deposition Method," *Advanced Studies in Theoretical Physics*, vol. 5, no. 4, pp. 171 - 183, 2011.

[57] F. J. Pern, B. To, C. Dehart, X. Li, S. H. Glick and R. Noufi, "Degradation of ZnO Window Layer for CIGS by Damp-Heat Exposure," in *SPIE PV Reliability Symposium*, San Diego, California, 2008.

[58] G. T. Koishiyev, J. R. Sites, S. S. Kulkarni, N. G. Dhere, "Determination of Back Contact Barrier Height in Cu(In,Ga)(Se,S)2 and CdTe Solar Cells," pp. 1 - 3, 2008.

[59] H. Tao, Z. Lin , W. Wang, I. Yang, and Z. Hong, "Preparation and Characteristics of CdS Thin Films by Dip-Coating Method using its Nanocrystal Ink," vol. 65, no. 9, pp. 1340-1343, May 2011.